

Regulating DNA Self-Assembly Dynamics with Controlled Nucleation

Shuoxing Jiang, Nibedita Pal, Fan Hong, Nour Eddine Fahmi, Huiyu Hu, Matthew Vrbanc, Hao Yan,* Nils G. Walter,* and Yan Liu*



Cite This: *ACS Nano* 2021, 15, 5384–5396



Read Online

ACCESS |



Metrics & More



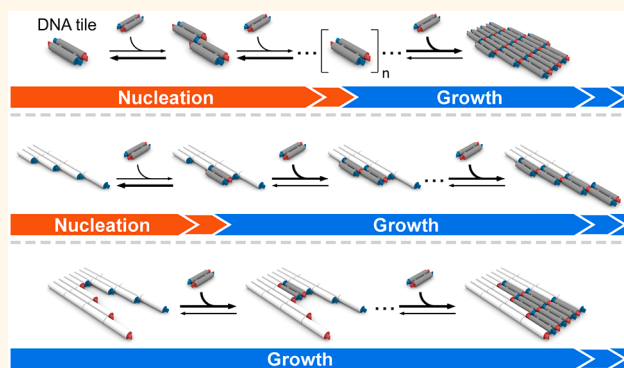
Article Recommendations



Supporting Information

ABSTRACT: Controlling the nucleation step of a self-assembly system is essential for engineering structural complexity and dynamic behaviors. Here, we design a “frame-filling” model system that comprises one type of self-complementary DNA tile and a hosting DNA origami frame to investigate the inherent dynamics of three general nucleation modes in nucleated self-assembly: unseeded, facet, and seeded nucleation. Guided by kinetic simulation, which suggested an optimal temperature range to differentiate the individual nucleation modes, and complemented by single-molecule observations, the transition of tiles from a metastable, monomeric state to a stable, polymerized state through the three nucleation pathways was monitored by Mg^{2+} -triggered kinetic measurements. The temperature-dependent kinetics for all three nucleation modes were correlated by a “nucleation–growth” model, which quantified the tendency of nucleation using an empirical nucleation number. Moreover, taking advantage of the temperature dependence of nucleation, tile assembly can be regulated externally by the hosting frame. An ultraviolet (UV)-responsive trigger was integrated into the frame to simultaneously control “when” and “where” nucleation started. Our results reveal the dynamic mechanisms of the distinct nucleation modes in DNA tile-based self-assembly and provide a general strategy for controlling the self-assembly process.

KEYWORDS: dynamic DNA nanotechnology, nucleation, molecular template, triggered growth, DNA origami



As the initial step of self-assembly, nucleation is ubiquitous and fundamental to many crystallographic and biological processes and determines the quality of crystallization and the efficiency of cellular functions.^{1–5} Highly regulated, nucleated self-assembly underlies many forms of intelligent behaviors in biological systems. A representative example is the polymerization of tubulins into microtubules during cell division,^{6–8} in which the γ -tubulin ring complex (γ TuRC) acts as a template and simultaneously controls when and where α - and β -tubulins nucleate.^{9,10} The molecular template not only carries the structural information that defines the geometry and direction of the downstream assembly but also regulates the nucleation pathway and polymerization kinetics. Despite the critical role of a molecular template in nucleated self-assembly, the choices of model systems for studying the nucleation process are limited. Ideally, a model system should fulfill the following requirements: structurally resemble natural counterparts, facilitate rational design, and allow for user-defined customization.

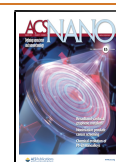
DNA nanotechnology provides a versatile platform for constructing bioinspired, nucleated self-assemblies.^{11–14} Most

DNA self-assembly protocols rely on DNA hybridization thermodynamics and result in static, equilibrium assemblies.^{15,16} It is more challenging to engineer DNA nanostructures that self-assemble isothermally and respond specifically to external stimuli.¹⁷ In the DNA nanotechnology toolbox, a suitable model system for studying nucleation is “templated DNA tile assembly”. DNA tiles can be assembled from a few single-stranded DNA oligonucleotides and further linked by single-stranded overhangs called “sticky ends” into 2D arrays or 3D crystals with distinct topological and geometric features.¹⁸ DNA tile-based self-assembly is a cooperative process,^{19,20} like tubulin polymerization. Monomeric tiles can barely nucleate under conditions where bivalent binding sites are lacking. The need for

Received: January 2, 2021

Accepted: March 8, 2021

Published: March 11, 2021



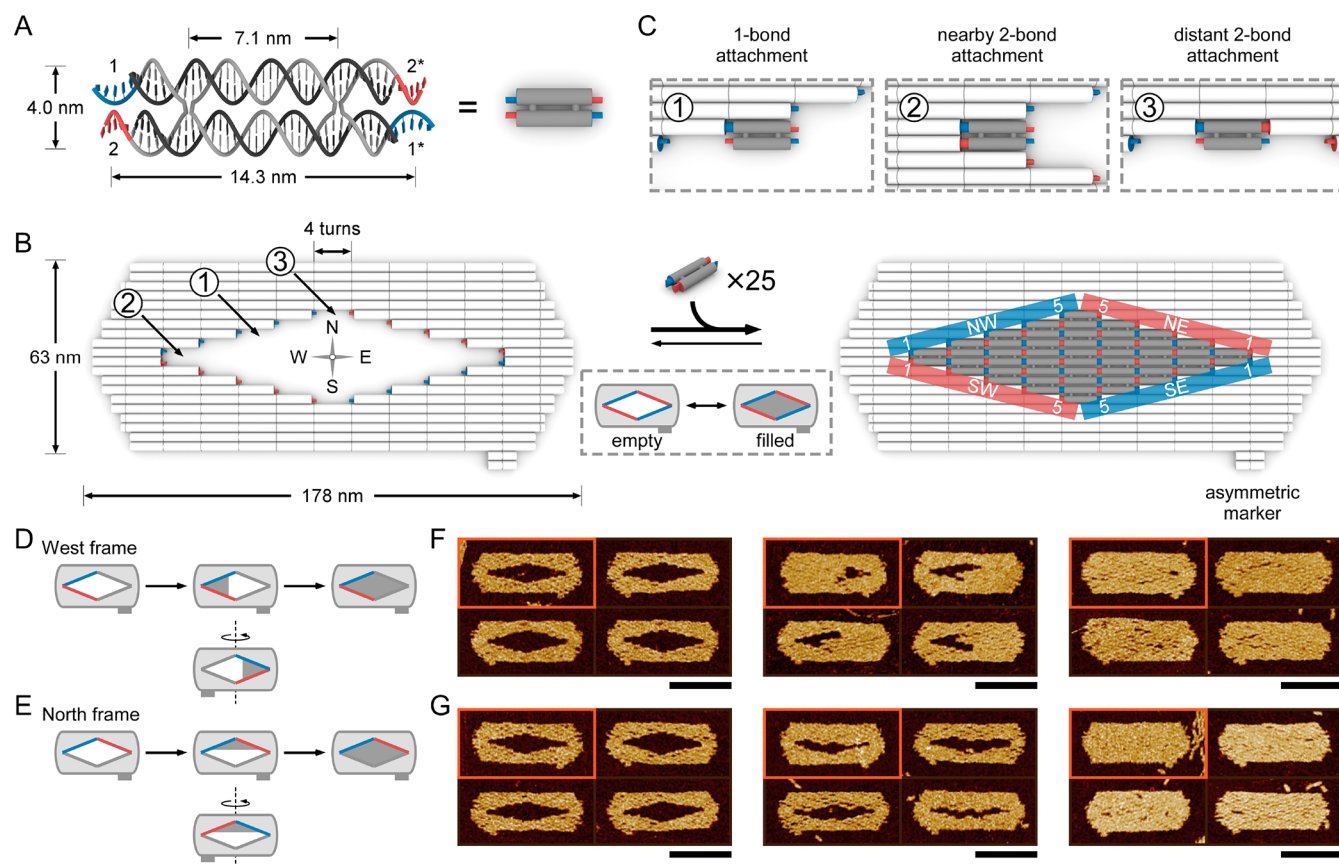


Figure 1. Structural design and AFM characterization of the frame-filling model system. The model system comprises two components: (A) a self-complementary DAE-E tile and (B) a rhombic template carried by a DNA origami frame, which can accommodate up to 25 tiles. Inset: a simplified schematic of the “empty” and “filled” states of the frame. Template edges that present sticky ends are red- or blue-colored to demonstrate the complementarity. The rhombic template presents three types of docking sites for a tile to attach: (1) 1-bond site on the edges, (2) nearby, or (3) distant 2-bond site at the vertices. Corresponding single-tile attachments in the three scenarios are illustrated in (C). (D and E) Simplified schematics of directed tile polymerization from designated vertices: West (D) and North (E). Edges without sticky ends are gray-colored. (F and G) AFM characterization of DNA tile assembly into the DNA origami frame. The DNA tiles nucleate from the West vertex (F) or the North vertex (G), respectively, and continue growing to fill the template. The majority of the frames ($\sim 75\%$) took the face-down orientation due to the intrinsic curvature. The frames taking the face-up orientation are marked with an orange box. Growth stops when the frame is filled with 25 tiles.

a nucleation stage in DNA tile-based self-assembly is evidenced theoretically and experimentally.^{20–23} Thus, it becomes feasible to regulate the tile assembly process by intervening in the nucleation stage. DNA origami²⁴ structures have been employed as “seeds” for templated DNA tile assembly.^{22,25–31} In such systems, the DNA origami seeds promote tile nucleation by diminishing both the nucleation energy and kinetic barriers. Notably, specific structural features such as geometry, rigidity, and complementarity can be customized in DNA tile and DNA origami, making them ideal building blocks to mimic complex molecular systems and regulate their dynamic behaviors. Moreover, natural systems achieve self-assembly regulation *via* complex biochemical circuits and responsive molecular templates. The former has been recapitulated by DNA tile-based assembly,^{23,32} while the latter has not yet been demonstrated.

Previous studies of DNA self-assembly dynamics generally simplified the measurement by designing a series of intermediate species and elementary steps along the self-assembly pathway.^{33–36} Compared with the elementary DNA self-assembly steps, such as oligonucleotide hybridization and single-tile attachment, nucleated self-assembly is more complicated as it involves multiple pathways with side reactions and produces

intermediate species. The nucleation of tiles in the presence of the seed can be broadly categorized into three modes based on the elementary assembly steps and the resulted nuclei: unseeded nucleation, facet nucleation, and seeded nucleation.^{37,38} Seeded nucleation is the most stable nucleation pathway as it starts with bivalent tile attachment, while facet and unseeded nucleation modes must go through one or more monovalent tile attachment steps before a bivalent site becomes available. Under a given experimental condition, different nucleation modes often interweave and compete with each other, complicating the quantification of kinetics. To monitor the dynamics of such systems, it is necessary to choose desirable conditions to differentiate the nucleation modes.

Here, we demonstrate control over the self-assembly of DNA tiles by tuning the tendency of nucleation. We designed a “frame-filling” model system that comprises a self-complementary tile and a rhombic template carried by a DNA origami frame. The template can be customized to favor a specific nucleation mode and a specific order of sequential tile attachments. Using the temperature ranges suggested by kinetic simulation, different nucleation modes were monitored individually by Mg^{2+} -triggered kinetic measurements with the competing nucleation modes inhibited. The kinetics of all three

nucleation modes showed dramatic temperature dependence, which could be qualitatively modeled as a “nucleation–growth” process. We further integrated an ultraviolet (UV)-responsive “gatekeeper” into the template to externally and simultaneously regulate “when” and “where” the tiles nucleated by UV light. This study expands the available strategies for building sophisticated dynamic self-assembly systems from nucleic acid building blocks. These dynamic systems have potential applications in mimicking the dynamic behaviors of their biological counterparts, building active nanophotonic devices through the directed assembly of plasmonic nanomaterials, and biosensing of molecular analytes.

RESULTS AND DISCUSSIONS

DNA Tile-Based Self-Assembly and its $[Mg^{2+}]$ -Dependence. A DAE-E tile motif³⁹ (D, double crossover; A, antiparallel; E-E, even number of helical half-turns between crossovers within the tile and between neighboring tiles) was chosen as the basic building block for this study (Figure 1A). Each tile carries four sticky ends with diagonal ones complementary to each other (1 pairs with 1*, 2 pairs with 2*). The self-complementary tile design ensures that the free energy changes for 2-bond attachments with two nearby or distant sticky ends are the same. For kinetic measurement, sticky end 1 was labeled with a 6-carboxyfluorescein (6-FAM) reporter to monitor tile assembly due to its sensitive response to DNA hybridization.^{40,41} For melting curve analysis, an additional reference sample with sticky ends 1 and 1* labeled with 6-FAM and tetramethylrhodamine (TAMRA), respectively, was included to correct the temperature dependence of 6-FAM. We used the identical core sequences of the tile from a previous study³⁶ but with weaker sticky ends to ensure that the tile formation was well-separated from lattice formation in a thermal annealing process, *i.e.*, tiles assembled hierarchically. Indeed, in 1 × TAE buffer containing 12.5 mM Mg^{2+} , the fluorescence melting curves along both annealing and melting ramps showed two well-separated transitions, and three isolated states could be identified: oligonucleotides, monomers, and lattices (Figure S1). Particularly, tiles formed at a temperature ~ 25 °C higher than that of lattice formation. Therefore, the monomeric state could be maintained over a relatively wide temperature range. Analyzing the concentration dependence of lattice melting (Figure S2) gave the standard enthalpy change ($\Delta H^\circ = 87.4 \pm 5.3$ kcal/mol) and entropy change ($\Delta S^\circ = 0.252 \pm 0.015$ kcal/mol) for lattice dissociation.

DNA Origami Frame Carrying a Rhombic Template. The DNA origami frame ($\sim 178 \times 63$ nm) used in this study was designed with a rhombic interior space (approximately 126 and 30 nm of the diagonal lengths) (Figure 1B). Each inner edge could present five sticky ends of the proper distance, and up to 25 tiles could be accommodated inside the template. To minimize the lattice mismatch between DNA origami frame and tile lattice²⁶ and to accommodate the shape and curvature of the tile lattice,⁴² the average spacing between neighboring crossovers of the frame was set to be 42 nucleotides (Figure S7), which was equivalent to the average crossover distance of the DAE-E tile lattice (four helical turns).⁴² Compared to traditional DNA origami designs with three helical turns per crossover and an ~ 2.69 nm interhelical distance,⁴³ a wider distance between neighboring helices (~ 3.05 nm) was observed in our frame design. Therefore, the width of two neighboring helices was ~ 6.10 nm in the frame design, which was expected to match the 6 nm spacing of the DAE-E tile lattice.⁴² The innermost layer of

the frame was constructed solely by staple strands to present the sticky ends for the tiles to attach. Sticky ends of the same sequence were assigned with the same coaxial stacking base to minimize energy inconsistency. The direction of the template was defined by compass direction: north (N), south (S), west (W), and east (E) (Figure 1B). Thus, the four inner edges were defined as NW, SW, NE, and SE edges, respectively. The template presented three types of docking sites for a tile to nucleate (Figure 1C). Tile attachment to the “nearby 2-bond” or “distant 2-bond” sites at the vertices could create two downstream 2-bond sites of the same type, nearby or distant. Tile attachment to the 1-bond sites along the edges could also create two 2-bond sites but of different types, one nearby and one distant.

It should be noted that the sticky ends presented by the two diagonal edges (NW vs SE and NE vs SW) are complementary to each other, which would cause severe aggregation of the origami frames if they are all present. Thus, only the adjacent two edges were assigned with sticky ends for seeded nucleation, while the other two were left with blunt ends. A “West frame” (W-frame) was designed with sticky ends on the NW and SW edges (Figure 1D), allowing seeded nucleation to initiate from the W vertex by two nearby sticky ends (1 and 2 on the tile); while a “North frame” (N-frame) was designed with sticky ends on the NW and NE edges (Figure 1E), allowing seeded nucleation to initiate from the N vertex by two distant sticky ends (1 and 2* on the tile). Both types of 2-bond attachments involve the hybridization of the same pairs of sticky ends, minimizing the free energy discrepancy induced by any sequence difference.

The morphologies of the frame before, during, and after tile polymerization were characterized by atomic force microscopy (AFM) (Figure 1F,G). A 55-nucleotide (nt) loop of the scaffold was left at the SE exterior corner of the frame as an asymmetric marker to differentiate the landing sides of the individual origami frames under AFM, so the identity of the four inner edges of the frame could be assigned unambiguously. The majority ($\sim 75\%$) of the frames took the face-down orientation (Figure S9), suggesting that the curvature of the frame agrees with the intrinsic curvature of the tile lattice.⁴² The tiles could nucleate at the designated vertices and continue to fill the rhombic template. Under optimal, high-concentration conditions, a 2-fold excess of tiles (50:1 molar ratio of tile to frame) could isothermally fill more than 90% of the frames (Figure S10). The incomplete filling is likely due to the intrinsic imperfection of origami formation,^{44–46} such as randomly missing staples. By strategically placing a pair of stopper sticky ends (3 nt each) at the terminal vertex (E or S vertex) where the 25th tile binds, tile polymerization could be effectively terminated when a frame was fully filled. Tile lattices that continuously grew out of the frame boundaries were very rare ($< 1\%$). The tile lattice in the W-frame was slightly more defective than that in the N-frame because the bivalent binding site on the W-frame is less accessible than that of the N-frame. The curvature and structural flexibility of the frame allow nucleation from the second pair of downstream sticky ends, leaving the designated starting position at the W-vertex vacant (Figure S11). This situation is not likely to occur for the N-frame. The programmability of DNA origami allows for user-defined customization to each binding site on the DNA frame pegboard, facilitating the rational design of various nucleation scenarios.

Modeling Nucleation Competition with Kinetic Simulation. Tile attachment with more sticky ends is thermodynamically more stable than that with only one sticky end.^{22,36,47}

A unseeded nucleation and growth

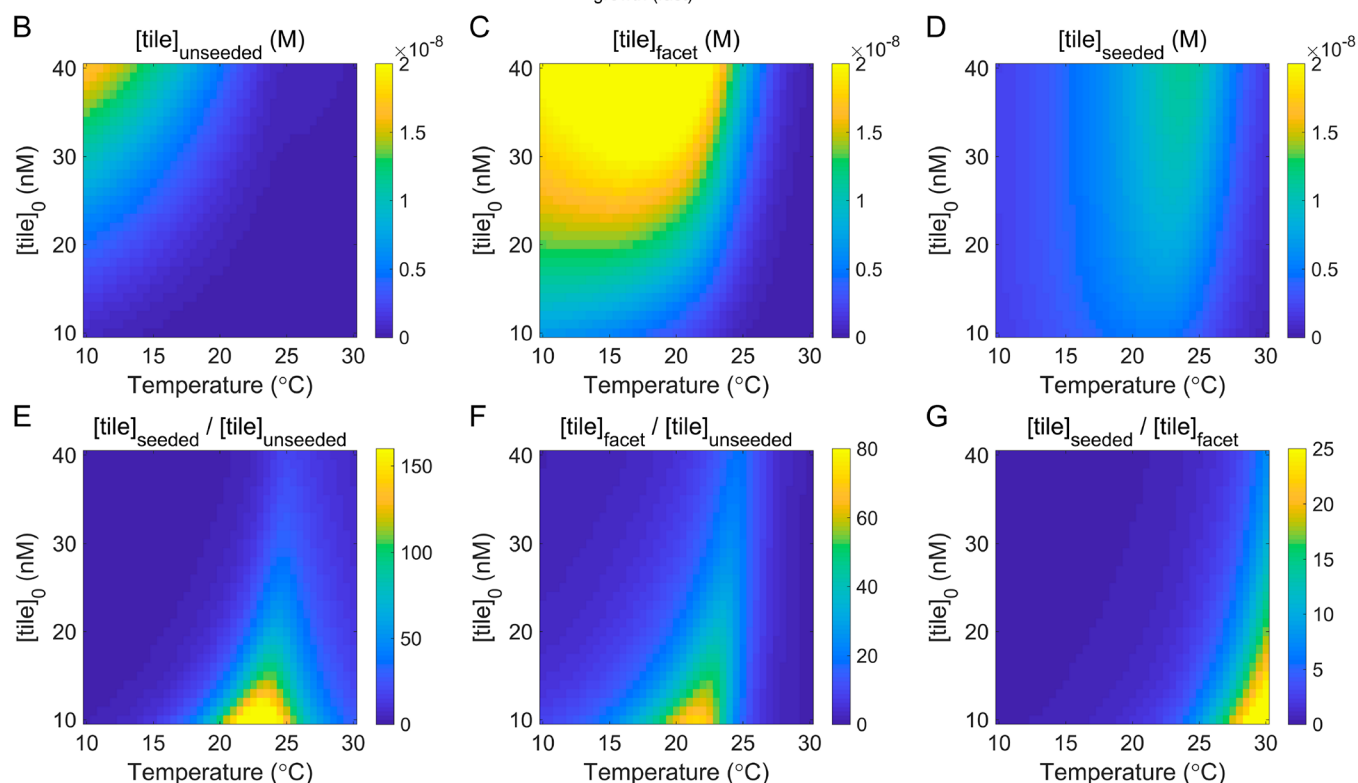
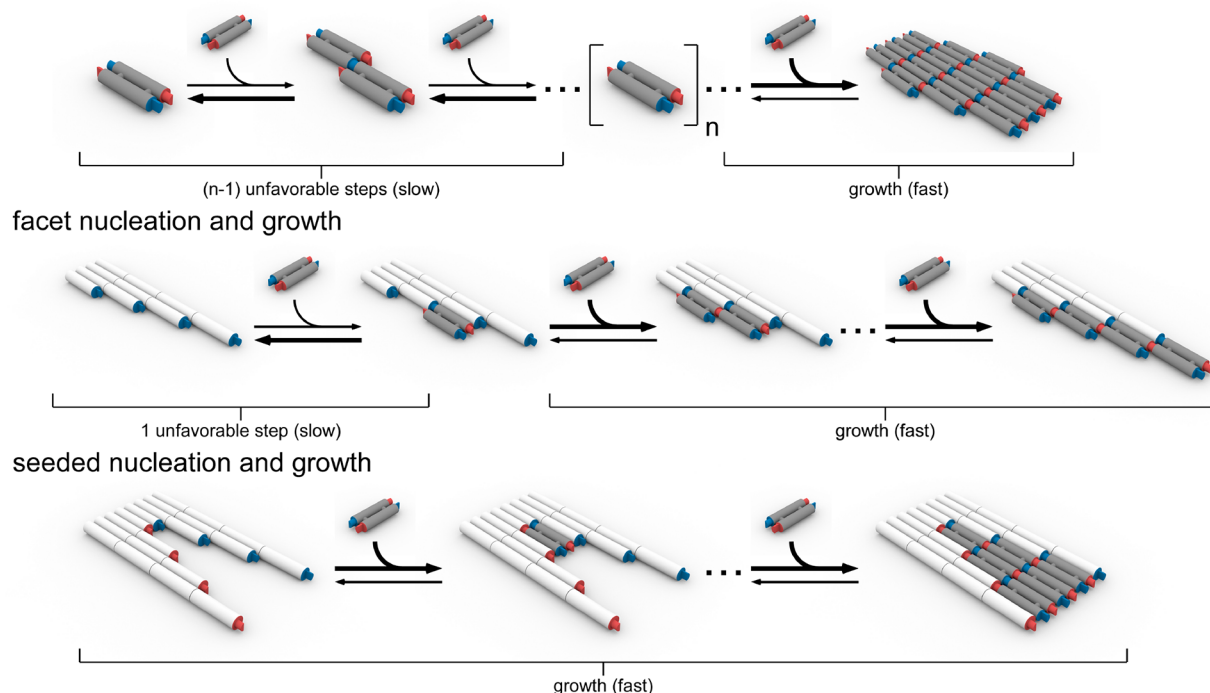


Figure 2. Schematic of the three possible nucleation pathways and their competition. (A) Three nucleation pathways are categorized on the basis of the number of 1-bond steps before reaching the critical nucleus. Tile attachment is unfavorable until forming a critical nucleus of n tiles. The bold arrows indicate the more favorable reaction direction. The elementary steps to reach the critical nucleus and the further growth thereafter can be described by an ordinary differential equation (ODE) model. Thermodynamic and kinetic parameters obtained from the previous studies were used to parametrize the ODE model (see details in the [Supporting Information](#)). The concentration of each species is the numerical solution of the ODE model. ODE simulation reveals the temperature dependence of different nucleation modes. (B–D) Heatmaps of the equilibrium concentration of the tiles consumed by unseeded (B), facet (C), and seeded (D) nucleation. (E–G) Heatmaps of the concentration ratio between any two nucleation modes.

However, in the absence of a nucleation seed, monomer tiles can only interact with each other with one sticky end, forming

dimers, trimers, *etc.* (Figure 2A). The multimers are likely to dissociate into monomers unless a critical nucleus of n -

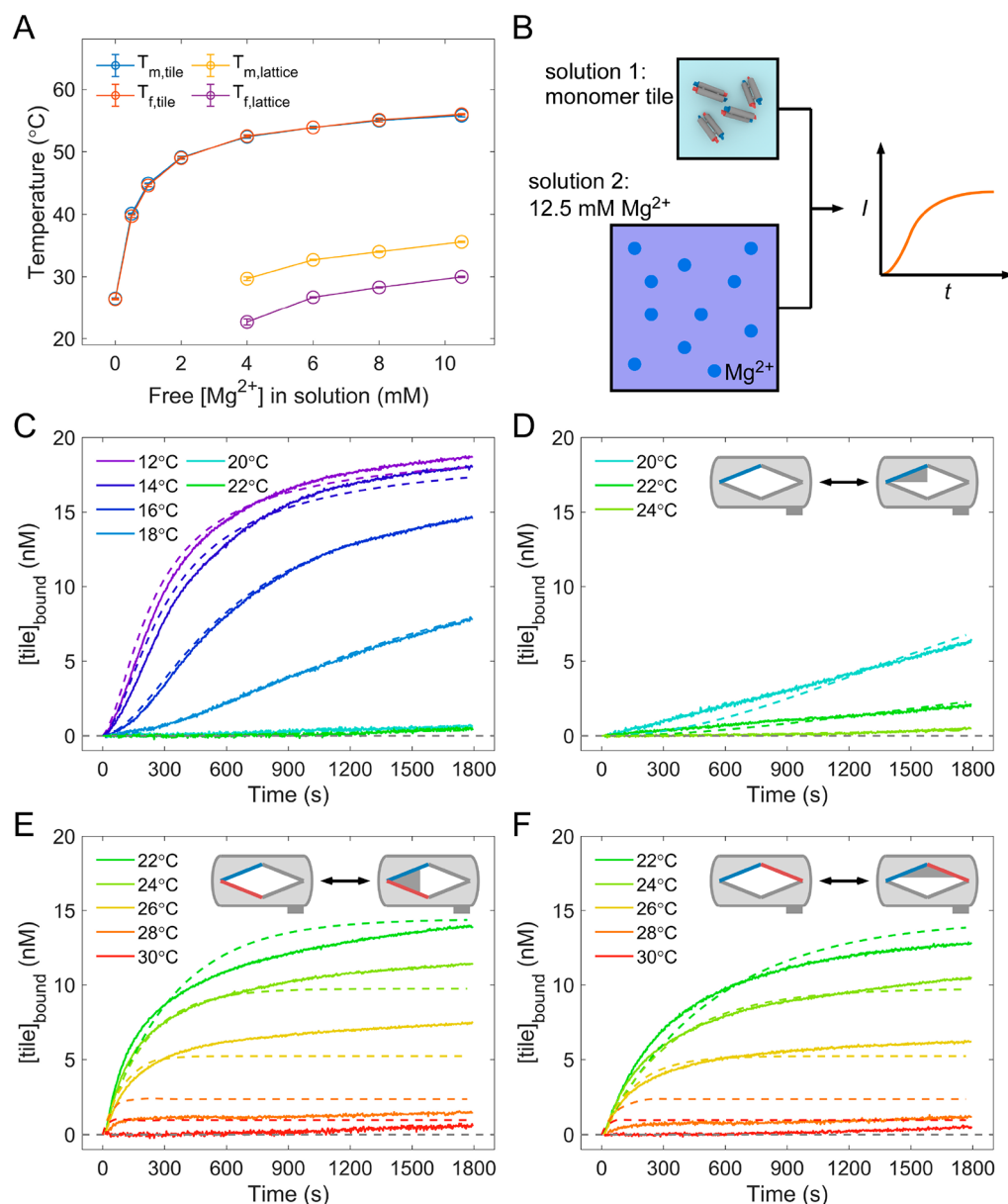


Figure 3. Mg^{2+} -triggered kinetic measurements of the unseeded, facet, and two types of seeded nucleation. (A) The formation temperature (T_f) and the melting temperature (T_m) of the self-complementary tile monomer and its lattice are both $[\text{Mg}^{2+}]$ -dependent. The tile formation and melting are essentially reversible, while the lattice melts at a higher temperature than its formation at each given $[\text{Mg}^{2+}]$. For all the $[\text{Mg}^{2+}]$ tested, tile formation and lattice formation are well-separated by $>20^\circ\text{C}$, which facilitates the preparation of metastable, monomeric tiles at room temperature in a solution containing low $[\text{Mg}^{2+}]$. (B) Experimental method for the measurement of unseeded nucleation and growth at arbitrary, constant temperatures. The assembly of metastable, monomeric tiles prepared in a solution containing low $[\text{Mg}^{2+}]$ (solution 1) was triggered by rapidly surging $[\text{Mg}^{2+}]$ to a high level by a buffer containing high $[\text{Mg}^{2+}]$ (solution 2) within seconds. For the measurement of facet and seeded nucleation, the corresponding frame was prediluted in solution 2. (C–F) Kinetic curves (solid line) and corresponding fitting (dashed line) for unseeded (C), facet (D), and two types of seeded nucleation seeded by W-frame (E) and N-frame (F) under constant temperatures. Kinetic curves measured under the same temperature are plotted using the same color. Inset: schematic illustrating the template design for facet and seeded nucleation.

mer) is reached. The nucleation number n is phenomenological, which was reported to be 2.5 at room temperature.²³ Once the nucleation barrier is overcome by spontaneous formation of the critical nucleus, the tendency of its downstream assembly is altered to favor a fast lattice growth. A nucleation seed provides a continuous growth frontier that mimics a critical nucleus, diminishing the kinetic barrier of nucleation. Therefore, in the presence of a nucleation seed, tiles can assemble through multiple pathways, either nucleating spontaneously (called unseeded nucleation) or growing directly onto the seed. In the

latter case, a free tile can either attach to the seed by two bonds (called seeded nucleation) or by a single bond and get “locked” by a subsequent, more stable bivalent tile addition (called facet nucleation) (Figure 2A). The preference of nucleation pathways is expected to depend on the experimental conditions.

To evaluate the preference of the three nucleation modes under experimental conditions, we made the following assumptions:

1. The formation of a complex in which every tile is attached by two bonds is considered successful nucleation, after which the assembly proceeds to the growth stage.
2. The difference between the three modes of nucleation is the number of 1-bond attachment steps required to form a critical nucleus.
3. In the growth stage, the nucleus can transform free tile(s) to bound tile(s) by 2-bond attachment and meanwhile grow larger.
4. No matter how large the lattice is, the thermodynamic and kinetic properties of an attached tile are exclusively determined by the number of sticky ends that are involved.
5. The joining or splitting of existing lattices are not considered contributors to lattice growth or dissociation in this model.

On the basis of Assumptions 1 and 2, the minimal numbers of 1-bond steps required to form a critical nucleus are 2, 1, and 0 for unseeded, facet, and seeded nucleation, respectively. Besides, parallel nucleation pathways involving dimer attachment were also considered in the model. Thus, the nucleation pathway can be dissected into elementary tile attachment or detachment steps between the starting species (free tile, seed), intermediate species (dimer, trimer, *etc.*), and product species (bound tile through certain nucleation pathways). Given the reversible nature of tile assembly, each species in the model can be generated or consumed. The concentration change of each species can be described by the kinetics of tile attachment or detachment using an ordinary differential equation (ODE) set (detailed model is given in the [Supporting Information](#)). The ODE set was parametrized with literature-reported thermodynamic and kinetic parameters obtained in $1 \times$ TAE buffer containing 12.5 mM Mg^{2+} .^{33,35,36} The numerical solution of the ODE set was calculated with a 0.8 nM initial seed concentration ($[\text{seed}]_0$), an initial free tile concentration ($[\text{tile}]_0$) range of 10–40 nM, and a temperature range of 10–30 °C. Under each combination of experimental conditions, the model calculated the equilibrium concentrations of tiles assembled through unseeded, facet, and seeded nucleation pathways ([Figure 2B–D](#)), which suggested the conditions that favor a specific nucleation mode. For example, a low temperature and high $[\text{tile}]_0$ favored unseeded nucleation since both conditions facilitated 1-bond attachment ([Figure 2B](#)). An elevated temperature inhibited unseeded nucleation as 1-bond attachment got more labile. Facet nucleation became the dominant nucleation pathway as 8-fold more sticky ends were available for the facet nucleation than the seeded nucleation in our W- or N-frame design ([Figure 2C](#)). Seeded nucleation became dominant at further elevated temperatures ([Figure 2D](#)) until the temperature exceeded the melting temperature of 2-bond attachment. The tile assembly yield dropped drastically thereafter. It should be noted that, although the ODE model recapitulates the competition between different nucleation pathways, it is a deterministic model based on the list of possible chemical reactions that are involved. Its performance is determined by the comprehensiveness of listed reactions and the accuracy of parameters and assumptions. Factors such as steric hindrance, the spatial arrangement of tiles, and the gradual change of structural flexibility were not parametrized in the current ODE model. As a result, the prediction might be biased (*e.g.*, the kinetics might be overestimated). To accurately

quantify these effects and implement them in the model, further research (*e.g.*, single-molecule kinetic measurement) is needed.

To experimentally monitor tile assembly through a specific nucleation pathway, the other competitive pathways must be inhibited. The ratio of yields between any two nucleation modes was calculated ([Figure 2E–G](#)), which suggested the optimal temperature range to carry out the kinetic measurement. For an experimental $[\text{tile}]_0$ of 20 nM, a peak ratio in seeded/unseeded and facet/unseeded was clearly shown as the temperature increased; the unseeded nucleation was best differentiated from both the facet and seeded nucleation at ~ 23 °C ([Figure 2E,F](#)). However, seeded nucleation was always accompanied by facet nucleation; the differentiation factor kept rising as the temperature increased ([Figure 2G](#)). As a major source of assembly error,^{48,49} facet error is stochastic and can hardly be eliminated without compromising the yield of seeded nucleation. As suggested by the ODE simulation, we chose the following temperature ranges for kinetic measurements: unseeded nucleation was monitored from 12 to 22 °C in the absence of the seed, and facet and seeded nucleation were monitored above 20 °C in the presence of the seed. ODE simulation provided a simple connection between the elementary tile assembly steps and the overall nucleation preference, which further guided the choice of experimental conditions. The temperature threshold suggested by the simulation was examined by the kinetic measurement.

Kinetics of Mg^{2+} -Triggered Tile Assembly. Both tile formation and lattice assembly transitions were $[\text{Mg}^{2+}]$ -dependent ([Figure 3A](#) and [Figure S3](#)). Reducing $[\text{Mg}^{2+}]$ to 2.5 mM trapped the tiles in the metastable, monomeric state at room temperature without detectable lattice formation. Considering the chelation ability of 2.0 mM EDTA in the buffer recipe, the effective $[\text{Mg}^{2+}]$ was ~ 0.5 mM to maintain a stable monomeric tile at room temperature. The corresponding annealing and melting curves only showed a single transition of tile formation at ~ 40 °C. Monomer tiles could be kept for 12 h without spontaneous nucleation ([Figure S4](#)), and they stayed structurally intact below 35 °C ([Figure S3B](#)). Further decreasing $[\text{Mg}^{2+}]$ to 2.0 mM deprived the structure integrity of tile at room temperature ([Figure S3A](#)), whereas increasing $[\text{Mg}^{2+}]$ broke the metastable state by promoting lattice formation ([Figure S3E–H](#)). Tuning $[\text{Mg}^{2+}]$ is a convenient strategy to induce the dynamic response of DNA nanostructures.^{50–53} The assembly of the preformed monomer tiles could be triggered by a rapid surge of $[\text{Mg}^{2+}]$. The hierarchy feature and $[\text{Mg}^{2+}]$ -dependence of DNA tile assembly facilitate the kinetic measurements under user-defined temperature and supersaturated conditions.

The tiles were preformed as concentrated monomers in a buffer containing 2.5 mM Mg^{2+} by annealing the mixture of strands from 90 to 26 °C. The temperature dependence of tile assembly was studied by Mg^{2+} -triggered kinetic measurement by rapidly surging $[\text{Mg}^{2+}]$ to 12.5 mM at a selected constant temperature ([Figure 3B](#)). The fluorescence enhancement of the 6-FAM reporter labeled at sticky end 1 was isothermally monitored in real-time. The yield of unseeded nucleation increased from $\sim 0\%$ to 96% as temperature decreased from 22 to 12 °C ([Figure 3C](#)). A lower temperature shifted the equilibrium of the tiles from the free state to the bound state. The kinetic curves were sigmoidal, showing a lag phase at the beginning, suggesting a slower nucleation stage before the faster growth stage. As predicted by the ODE model, unseeded growth was inhibited above 22 °C. As 1-bond attachment got more

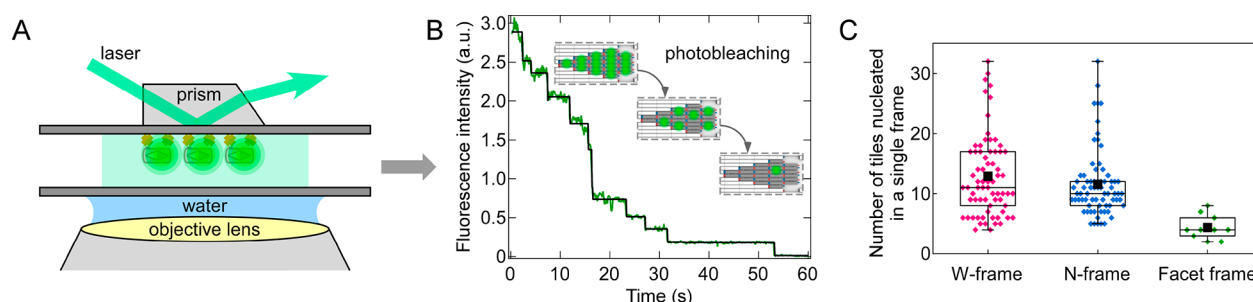


Figure 4. Quantification of the number of tiles nucleated per single frame as derived from stepwise photobleaching counting of single-fluorophore labeled tiles. (A) Schematic overview of the tile counting in every single frame by single-tile photobleaching. (B) Example single-tile stepwise photobleaching trajectories (green) of W-frame with respective detected steps (black lines). (C) Box-and-whisker plots revealing an average number of tiles nucleated into W-, N-, and facet frames of 13, 12, and 4, respectively, as measured by stepwise photobleaching counting. The boxes extend from the 25% to 75% confidence values, and the whiskers extend from the minimum to the maximum values. The average number of tiles nucleated in each frame type is presented as a small solid black square. The black line denotes the median.

labile at elevated temperature, unseeded nucleation that involved more 1-bond steps was inhibited first (Figure 3C).

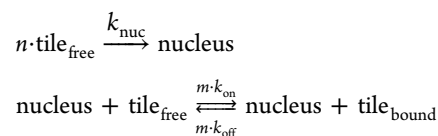
Facet nucleation was monitored from 20 to 24 °C in the presence of the origami frame presenting five sticky ends on the NW edge, *i.e.*, no bivalent site was provided (Figure 3D). The facet assembly was essentially eliminated above 24 °C. Compared to the current design, more sticky ends organized along a more extended facet would further favor facet nucleation, making facet nucleation control more difficult.

The seeded assembly was monitored from 22 to 30 °C in the presence of the W-frame (Figure 3E) or the N-frame (Figure 3F). Both scenarios' yields were almost identical, suggesting equivalent thermostability, consistent with the corresponding melting curves (Figure S5) and AFM characterization (Figure S11). No lag phase was observed in either case of the seeded nucleation, suggesting that the presence of the seed eliminated the nucleation stage and tiles started with the growth stage with every following step *via* 2-bond interaction. At 30 °C, a lag phase corresponding to the nucleation stage was observed due to the reduced thermostability of bivalent attachment at an elevated temperature (T_m was estimated as 29.1 °C for an experimental $[\text{tile}]_0$ of 20 nM, extrapolated from Figure S2). This temperature threshold was ~8–10 °C higher than that for the unseeded assembly (~20 °C). Therefore, in a narrow temperature range of 24–26 °C, the seeded assembly was the dominant process, as both unseeded and facet assembly were effectively inhibited. Taking advantage of the temperature dependence of nucleation and customized frame design, tile assembly can be guided to take a specific pathway. Interference between nucleation modes can be effectively avoided.

Distribution of Tile Numbers within Individual Frames Analyzed by Stepwise Photobleaching Counting. The distribution of tiles within individual frames was assessed by stepwise photobleaching counting (Figure 4A). Both W-frame and N-frame showed similar yields and distributions of tile numbers, consistent with our bulk measurements. For stepwise photobleaching experiments, each origami frame was labeled with eight Atto647 fluorophores (Figure S8) and each DNA tile was labeled with a single Cyanine 3 (Cy3) dye (Table S5). For surface immobilization, each frame was modified with five 5'-biotinylated staple strands protruding on the S outer edge. The DNA tiles were preassembled with the frames at a stoichiometric ratio (25:1) before each experiment, and all single-frame traces were collected at room temperature (detailed experimental steps and analysis procedures are given in the Materials and Methods section). Counting the photobleaching steps as Cy3 fluores-

cence intensity reduced over time (Figure 4B and Figure S12) revealed the number of tiles assembled within a single origami frame. We observed that, averaged from ~70 frames, ~13 tiles were assembled into the W-frame whereas ~12 tiles were assembled into the N-frame (Figure 4C and Table S4). The observed low assembly yield for facet nucleation (~4 tiles, calculated from ~10 frames) corroborates the low thermostability of the monovalent nucleation step (Figure 4C and Table S4). Although each frame can accommodate up to 25 tiles, the observed ~50% assembly yield can be attributed to the 3 orders of magnitude lower concentration used in the stepwise photobleaching experiments than the bulk measurements. Additionally, premature photobleaching of the fluorophores might lead to an underestimation of the tile numbers assembled in each frame. Still, the observations that the W- and N-frames showed similar assembly behaviors in contrast to the much less efficient facet nucleation are consistent with our ensemble kinetic studies.

Unified Kinetic Model of Nucleated Tile Assembly. To correlate the kinetic curves of each nucleation modes with the kinetics of elementary tile attachment, we proposed a simplified kinetic model, which describes nucleated tile assembly in two steps: nucleation and growth, as follows:



in which n is the empirical nucleation number and m is the growth coefficient, which defines the number of tiles that can simultaneously grow onto a nucleus. k_{nuc} was defined as $2 \times 10^5 \text{ M}^{1-n} \cdot \text{s}^{-1}$ for the rate constant of monomer tile nucleation.²³ Both k_{on} and k_{off} at an arbitrary temperature could be calculated from the thermodynamic ($\Delta H^\circ = -87.4 \text{ kcal/mol}$ and $\Delta S^\circ = -0.252 \text{ kcal/mol}$) and kinetic³⁶ ($\ln A = 26.7$ and $E_a = 7.6 \text{ kcal/mol}$) parameters of 2-bond attachment. In the fitting process, all parameters except for n and m were prescribed. For seeded nucleation fitting, since there was no lag phase, only the growth step was used and only the m value was obtained. Different nucleation modes have different m values. In the absence of a seed, tiles assemble into nanotubes with a mean circumference of 6 tiles,^{23,42} while in the presence of a facet, the attachment of a tile can create 1–2 bivalent binding sites. Given that the model is more sensitive to n , which defines the reaction order of the

Table 1. Fitted Parameters for Nucleation Modeling

unseeded nucleation ^a			facet nucleation ^a			seeded nucleation ^b		
temperature (°C)	<i>m</i> (assumed)	<i>n</i> (fitted)	temperature (°C)	<i>m</i> (assumed)	<i>n</i> (fitted)	temperature (°C)	<i>m</i> (W-frame, fitted)	<i>m</i> (N-frame, fitted)
12	6.0	2.13	20	1.0	1.21	22		
14	6.0	2.16				24		
16	6.0	2.24	22	1.0	1.29	26	2.92	1.76
18	6.0	2.36				28		
20	6.0	2.53	24	1.0	1.38	30		
22	6.0	2.55						

^aBoth unseeded and facet nucleation were analyzed by fitting *n* with the “fminunc” function in MatLab. No standard deviation was obtained. ^bSince only the growth step was used for seeded nucleation fitting, *m* values were obtained by fitting all kinetic curves with the “fminunc” function in MatLab using the same *m*.

nucleation step, *m* was assumed as 6.0 and 1.0 for the unseeded and facet nucleation to fit *n*, respectively.

With *n* and *m*, the kinetic model qualitatively reproduced the characteristic features of each nucleation mode, including both the characteristic shape of the kinetic curves and the temperature dependence of assembly yield. On the basis of the fitting of different nucleation modes, *n* fell in different ranges: between 2 and 3 for unseeded nucleation, between 1 and 2 for facet nucleation, and null for seeded nucleation (Table 1). On the basis of the model, *n* can be considered the minimal nucleus that allows bivalent tile attachment. For unseeded nucleation, the fourth tile attachment to a trimer is bivalent; the dimerization of two dimers to form a tetramer is also bivalent. The values of *n* for these two scenarios are 3 and 2, respectively. The noninteger *n* values for unseeded nucleation indicated that both pathways, as mentioned above, could be taken. The value of *n* increased at an elevated temperature, indicating a higher order of nucleation step and more difficult nucleation. The frame design for facet nucleation geometrically mimicked a set of preformed tile dimers. Thus, the empirical reaction order of the nucleation step was reduced to the range 1–2 (1.3 ± 0.1). The frame with a seeded nucleation site further reduced *n*, as it essentially mimicked a preformed tile trimer that required no further reaction step to form a bivalent binding site. As a result, the initial lag phase in the kinetic curve disappeared (Figure 3E,F). The nucleation number obtained here is consistent with the phenomenological stoichiometry of nucleation obtained from a catalyzed tile assembly system.²³ It is affected by temperature and nucleation seed and determines the tendency of nucleation.

The fitted *m* values were 2.92 and 1.76 for W- and N-frame-guided nucleation, respectively. It is noted that the *m* value of the W-frame is ~1.5-fold more than that of the N-frame, suggesting that other parallel pathways may exist (e.g., tile attachment starting from the second pair of sticky ends downstream the vertex) and facilitate seeded nucleation on the W-frame. For this reason, the kinetic curves for seeded nucleation mediated by the W-frame could not be quantitatively fitted by the model. This possible pathway was confirmed by removing the bivalent site on the W-vertex of the W-frame (Figure 5A). The resultant kinetics was reduced in rate and yield but not inhibited by this modification. In contrast, this pathway was prohibited by a longer distance in the N-frame (Figure 5B). Tile attachment is rather strictly ordered for the N-frame, i.e., downstream tiles rely on the upstream tiles to attach. The order of assembly is essential for the information propagation system. By evaluating *m*, hidden nucleation pathways promoted by the closer organization of binding sites can be identified.

Triggering Tile Assembly by Activating Photo-Responsive Seed. DNA tile assembly has been demonstrated to be regulated by a strand displacement circuit that mimics the biochemical network in biological systems,^{23,32} in which the regulatory module is implemented on every building block. A parallel regulation strategy is through external regulation by implementing the regulatory module onto the seed structure that controls the initiation of assembly. In this study, we have discovered that distinct temperature dependence of different nucleation modes facilitates the differentiation of seeded nucleation from unseeded nucleation. However, to implement the regulation module onto the seed, it would be more desirable to further differentiate seeded nucleation from facet nucleation. To this end, a photo-responsive seed was designed on the basis of the N-frame to provide an additional gate to control when and where nucleation starts (Figure 5C). The subtle temperature dependence of nucleation was utilized to design such a nucleation seed that can be activated externally and conditionally. The only seeded nucleation site on the N-frame was initially blocked by its complementary sequence covalently connected by a photocleavable 1-(2-nitrophenyl)ethyl linker. Subsequent assembly was triggered by cleaving the photocleavable linker by UV irradiation to release the blockers from the seeded nucleation site. The real-time triggering of nucleation was demonstrated in bulk measurement at 24 °C (Figure 5D,E). Kinetic curves were recorded in the presence of either the inactive seed or the activated seed. During the experimental time, with the inactive seed, increasing $[Mg^{2+}]$ alone could not trigger the growth of tiles, even though the tiles are unmodified and ready-to-assemble, as the temperature was set high enough to inhibit both unseeded and facet nucleation, while with the activated seed, increasing $[Mg^{2+}]$ triggers tile growth without any lag phase. The inactive seed could be activated at any time by a brief UV irradiation. Once activated, tiles started to grow onto the seeds, reaching a similar yield as with the preactivated seeds within the same time. This triggering strategy exploits the thermodynamic preference of different nucleation pathways. It does not require any modification on the tile and is orthogonal and compatible with the previously reported DNA circuit strategy. Other chemical modifications for seed activation can also be integrated into our template design. Integrating these regulation strategies could facilitate more sophisticated control over the nucleated tile assembly.

CONCLUSIONS

As the initial step of self-assembly, nucleation plays a significant role in determining the quality and fate of self-assembly. Based on the pathways to form a critical nucleus, the nucleation process can be categorized into three modes: unseeded, facet,

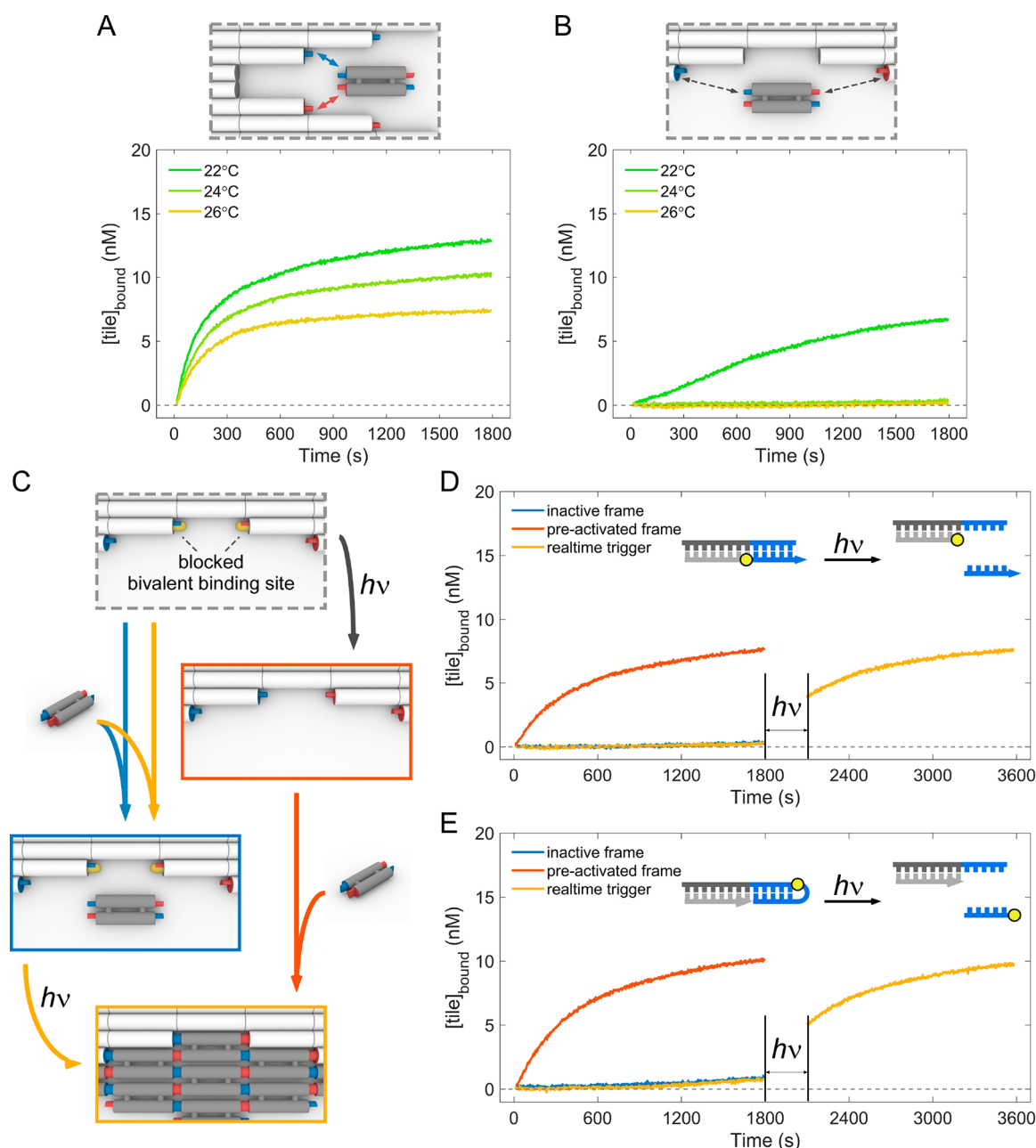


Figure 5. Structural design of photo-responsive tile nucleation. (A) Nucleation is not completely inhibited by truncating the only bivalent nucleation site on the W-frame, indicating the existence of other parallel nucleation pathways. (B) Nucleation is inhibited by truncating the only bivalent nucleation site on the N-frame, suggesting that this bivalent site is the only starting position for tiles to nucleate. (C) Schematic of a triggering strategy of tile assembly: by integrating a UV-responsive blocking module onto the N-frame, tile assembly can be triggered in response to UV radiation. When the only bivalent site is blocked on the N-frame, tiles can hardly nucleate *via* facet nucleation (blue arrow). If the frame is preactivated by UV radiation and the bivalent nucleation site is exposed, tiles can readily nucleate and assemble into the frame *via* seeded nucleation (red arrow). Therefore, tile assembly can be triggered in real time by UV radiation (yellow arrow). (D) First design strategy of the UV-responsive trigger and the corresponding kinetic curves at 24 °C. The short, 5 nt sticky end at the bivalent binding site is initially blocked by its complementary blocker sequence. UV radiation cleaves the photocleavable spacer (yellow circle) and leads to a spontaneous release of the 5 nt blocker strand. (E) Second design strategy of the UV-responsive trigger and the corresponding kinetic curves at 24 °C.

and seeded nucleation. If more unfavorable steps are involved to form the critical nucleus, the intermediates in the nucleation step are thermodynamically less stable and more susceptible to break down under an elevated temperature. Guided by the kinetic simulation, which describes the preference of nucleation modes at any given temperature, we experimentally verified the temperature dependence of different nucleation modes by Mg^{2+} -triggered kinetic measurements. The experimental results

were qualitatively described by the nucleation–growth model. Furthermore, a photo-responsive seed was constructed to achieve precise temporal and spatial control of DNA tile growth with an external regulation strategy.

Our results presented here elucidate the origin of the thermodynamic and kinetic difference between homogeneous and heterogeneous self-assembly. Controlling nucleation guides the self-assembly system to favor specific pathways to obtain

distinctly different assembly results and allows for more efficient, dynamic regulation. The major challenge for implementing complex dynamic assembly in the test tube lies in handling side reactions. Our experimental results could hopefully enhance the prediction of the actual assembly process under various experimental conditions. Finally, as a general understanding of nucleation, our approach is applicable to the quantification of nucleation tendency in other nucleated self-assembly systems in nature. For example, the spontaneous polymerization of α - and β -tubulins into microtubules can be considered the unseeded nucleation of an anisotropic building block with distinct lateral and longitudinal interactions.⁹ The γ TuRC is analogous to the facet frame used in this study, which provides multiple monovalent binding sites for longitudinal interactions.¹⁰ The growing end of the microtubule (GTP cap) is more analogous to the seeded frame, which provides multiple bivalent binding sites for lateral and longitudinal interactions.⁵⁴ The nucleation tendency of other nucleated self-assembly systems such as actin filaments, intermediate filaments, amyloid fibril, and a tobacco mosaic virus (TMV) protein tube can also be analyzed and compared by the empirical nucleation number. The information gained here using the model system is potentially useful to provide a deeper understanding of the nucleated self-assembly processes in nature.

MATERIALS AND METHODS

Monomer Tile Preparation. DNA strands for the self-complementary tile were purchased from Integrated DNA Technologies (IDT). Unmodified and 6-FAM-modified strands were purified by denaturing polyacrylamide gel electrophoresis (PAGE). TAMRA-modified and Cy3-modified strands were purified by IDT using high-performance liquid chromatography (HPLC) and used as received. Detailed DNA sequences are shown in Table S5. The concentrations of strands were calculated from the ultraviolet (UV) absorbance at 260 nm (A₂₆₀) in deionized water using the extinction coefficients provided by IDT. To prepare the monomer tile solution, equal molar amounts of DNA strands were mixed at a final concentration of 500 nM in 1 × TAE buffer (Tris base 40 mM, acetic acid 20 mM, EDTA-Na₂·12H₂O 2 mM) containing 2.5 mM (CH₃COO)₂Mg·4H₂O and then annealed from 90 to 26 °C at 1 °C/min. The annealing procedure was processed with an automated polymerase chain reaction (PCR) thermocycler (Mastercycler Pro, Eppendorf). The sample was held at 26 °C by the thermocycler until use. The monomer tile was freshly prepared before the measurements and immediately used after preparation to prevent spontaneous nucleation.

Origami Preparation. Single-stranded M13mp18 DNA was purchased from Bayou Biolabs (P-107) at 1 g/L in 1 × TE buffer (10 mM Tris-HCl, 1 mM EDTA, pH 8.0). The concentration of the M13mp18 strand was calculated on the basis of the mass concentration (microgram/microliter) converted from A₂₆₀.

Staple strands were categorized on the basis of their positions and functions within the DNA origami: core staples folding the M13mp18 DNA scaffold into the designed geometry, sticky end staples presenting the sticky ends at the growth frontier, and adaptor staples bridging the scaffold and the sticky end staples. Core staples, adaptor staples, and biotinylated staples (sequences listed in Tables S6, S7, and S9) were purchased unpurified from IDT and used as received. Sticky end staples (sequences listed in Table S8) were purchased unpurified from IDT and purified by denaturing PAGE. Atto647-modified and photocleavable-linker-modified strands (sequences listed in Tables S9 and S10) were purchased from IDT and purified by IDT using HPLC. Each origami design was prepared by mixing the M13mp18 scaffold with the corresponding staples at final concentrations of 10 nM M13mp18 scaffold, 50 nM core staples, 50 nM adaptor staples, and 100 nM sticky end staples in 1 × TAE/Mg²⁺ buffer (Tris base 40 mM, acetic acid 20 mM, EDTA-Na₂·12H₂O 2 mM, (CH₃COO)₂Mg·4H₂O 12.5 mM) and then being annealed from 90 to 25 °C in ~6 h. The annealing procedure

was processed with an automated PCR thermocycler (Mastercycler Pro, Eppendorf). The annealing procedure was as follows: the sample was first heated up to 90 °C; then, the temperature was reduced from 90 to 78 °C at 1 °C/min, from 78 to 58 °C at 1 °C/15 min, and from 58 to 25 °C at 1 °C/min. The sample was held at 25 °C by the thermocycler until use.

Fluorescence Thermal Curves. Fluorescence thermal curves were measured in optical tube strips using an Mx3005P quantitative PCR system (Agilent Technologies), a PCR thermocycler equipped with a real-time, fluorescence 96-well plate reader. To evaluate the concentration dependence of the melting temperature (T_m) of the tile lattice, the tile was prepared at final concentrations of 100–800 nM in 1 × TAE/Mg²⁺ buffer. To evaluate the effect of [Mg²⁺] on the thermostability of DNA tile and its lattice, the tile was prepared at a final concentration of 500 nM in 1 × TAE buffer containing 2.0–12.5 mM Mg²⁺. Sticky ends 1 and 1* of the tile were modified with 6-FAM (FRET donor) and TAMRA (FRET acceptor), respectively. The mixtures of the strands (30 μ L) containing only the donor (the strand labeled with TAMRA was replaced with an unlabeled strand of the same sequence) or both the donor and acceptor were pipetted in the tubes, covered and sealed with optical transparent caps, and placed in the thermocycler. The fluorescence intensity of 6-FAM emission was monitored at 522 nm with excitation at 495 nm at 1 min intervals throughout the thermal program. Unless otherwise noted, the preannealed samples in the thermocycler were first held at 25 °C for 30 min and heated to 80 °C at +0.1 °C/min. After heating to 80 °C, the samples were held for 10 min, and then, the temperature was reduced from 80 to 25 °C at −0.1 °C/min.

Kinetic Measurement. The fluorescence change over reaction time was monitored with a Nanolog fluorometer (Horiba Jobin Yvon). Nucleation kinetics was monitored in a quartz cuvette (Starna cells, 16.100F-Q-10/Z15) with a total reaction volume of 120 μ L. To monitor the kinetics of unseeded nucleation, 4.8 μ L of the monomer tile solution (500 nM) was mixed with 115.2 μ L of 1 × TAE/Mg²⁺ buffer (final tile concentration of 20 nM). Efficient mixing was achieved by pipetting 60 μ L volume 10 times in 3 s. To monitor the kinetics of facet or seeded nucleation, 9.6 μ L of the origami frame (10 nM) was prediluted into 105.6 μ L of 1 × TAE/Mg²⁺ buffer before the monomer tile solution was mixed. The parameter settings of the fluorescence measurements were as follows: 497 nm excitation, 1 nm excitation slit, 520 nm emission, 15 nm emission slit. The excitation slit was minimized to reduce exposure of the samples to the excitation light and thus prevent photobleaching of the dye molecules (especially at low concentrations). The emission slit was 15 nm wide to improve the emission light intensity (signal level). The detector was cooled to minimize noise. The signal was collected from 0 to 1800 s with 0.5 s integration time and 3 s intervals. Kinetic measurements were repeated 4–6 times at each temperature and recorded at 4–6 different temperatures for each nucleation mode. The sample temperature was maintained by a water circulating bath connected to the cuvette holder.

Atomic Force Microscopy (AFM) Characterization. For AFM imaging, 10 μ L samples (origami concentration of 0.8 nM) were deposited onto a freshly cleaved mica surface (Ted Pella) and 60 μ L of 1 × TAE/Mg²⁺ buffer was added to allow the sample to spread out for 2 min. The solution was then removed by blowing the mica surface with compressed air. The mica surface was washed twice with 60 μ L of 1 × TAE/Mg²⁺ buffer to minimize the imaging background from excess staples. After the wash, 2 μ L of NiCl₂ solution (100 mM) was added to assist adsorption. Then, 60 μ L of 1 × TAE/Mg²⁺ buffer was added onto the AFM tip. The samples were imaged in “ScanAsyst in Fluid” mode with a ScanAsyst-liquid+ tip on the Dimension FastScan AFM (Bruker).

Single-Molecule Tile Counting. Total internal reflection fluorescence microscopy (TIRFM) was employed to quantitatively assess the number of tiles assembled in a single DNA origami frame. The details of the experimental setup have been described elsewhere.⁵⁵ Briefly, a 532 nm green laser from CrystalLaser (CL532-050-L) and a 638 nm red laser from Coherent (OBIS 637) were used to excite Cy3 and Atto647 fluorophores, respectively. The fluorescence emission was collected by a 60×, 1.2 high-numerical aperture water immersion

objective from Olympus (Olympus UPlanApo) and then split into two channels for Cy3 and Atto647 by a pair of dichroic mirrors and reflective mirrors (Thorlabs) before projecting onto two halves of an sCMOS camera (ORCA-Flash4.0) from Hamamatsu. The fluorescence intensity vs time traces were collected as movies at 100 ms time resolution. The typical length of data collection was ~3–4 min. The intensity vs time traces were extracted using MATLAB scripts.

To start with, 0.8 nM origami frames were mixed with 20 nM tiles in 1 × TAE buffer with 12.5 mM MgCl₂ (pH 8.0) at 24 °C and cooled down to 18 °C over an hour. Then, the mixture was incubated at 18 °C for at least 30 min, allowing the nucleation to reach equilibrium. Next, the mixture was loaded onto a clean PEGylated quartz slide with a microfluidic channel. Each DNA origami frame was labeled with five biotin molecules for immobilization on a streptavidin-coated quartz slide through the biotin–streptavidin interaction. The detailed steps of surface functionalization and the construction of microfluidic channels have been described elsewhere.⁵⁶ Excess unbound frames and tiles were flushed away with buffer (1 × TAE containing 12.5 mM MgCl₂, pH 8.0). Surface-distributed DNA origami frames were detected by monitoring the fluorescence from the Atto647 fluorophore. Each DNA origami frame carried eight Atto647 fluorophores. For Atto647 excitation, the power of the 638 nm red laser was kept at ~15 mW. 1 × TAE (pH 8.0) supplemented with 12.5 mM MgCl₂ was used as an imaging buffer, and all data were acquired at a room temperature of ~18 °C. The quantification of the single Cy3 labeled tiles nucleated within a single DNA origami frame was achieved by counting the associated single-molecule photobleaching steps. As each Cy3 molecule was stochastically photobleached, the fluorescence intensity decreased in a stepwise fashion. The height of each step corresponds to a single or multiple overlapping Cy3 photobleaching events, and the total step count per trace corresponds with the number of tiles nucleating at that spot in the field of view (representing a single DNA origami frame). Thus, the total number of photobleaching steps yields the total number of tiles nucleated within a single DNA origami frame. Stepwise photobleaching analysis was performed by using a code written and developed in Python.⁵⁷ For photobleaching Cy3, the 532 nm green laser power was kept at ~7 mW so that all fluorophores were photobleached within 4–5 min (~3000 frames), a typical trajectory length for our data collection.

ASSOCIATED CONTENT

Supporting Information

The Supporting Information is available free of charge at <https://pubs.acs.org/doi/10.1021/acsnano.1c00027>.

Figures of cooling and heating curves, linear fitting of the concentration-dependent T_m , stability test, baseline for photobleaching correction, detailed design of the DNA origami frame for kinetic measurements and single-molecule tile counting, AFM characterization, and representative single-tile stepwise photobleaching trajectories, tables of experimentally measured T_m values, thermodynamic and kinetic parameters, species selected for the ODE model, quantitative analysis of single-tile stepwise photobleaching experiment, sequences of the oligos composing the DNA tile, sequences of the staple strands composing the DNA origami frame, and discussions of kinetic curve normalization and kinetic simulation by the ODE model (PDF)

AUTHOR INFORMATION

Corresponding Authors

Hao Yan — Center for Molecular Design and Biomimetics at the Biodesign Institute, and School of Molecular Sciences, Arizona State University, Tempe, Arizona 85287, United States; orcid.org/0000-0001-7397-9852; Email: hao.yan@asu.edu

Nils G. Walter — Single Molecule Analysis Group, Department of Chemistry, University of Michigan, Ann Arbor, Michigan 48109, United States; orcid.org/0000-0002-7301-1275; Email: nwalter@umich.edu

Yan Liu — Center for Molecular Design and Biomimetics at the Biodesign Institute, and School of Molecular Sciences, Arizona State University, Tempe, Arizona 85287, United States; orcid.org/0000-0003-0906-2606; Email: yan_liu@asu.edu

Authors

Shuoxing Jiang — Center for Molecular Design and Biomimetics at the Biodesign Institute, and School of Molecular Sciences, Arizona State University, Tempe, Arizona 85287, United States; orcid.org/0000-0002-9235-6447

Nibedita Pal — Single Molecule Analysis Group, Department of Chemistry, University of Michigan, Ann Arbor, Michigan 48109, United States; orcid.org/0000-0001-8172-1851

Fan Hong — Center for Molecular Design and Biomimetics at the Biodesign Institute, and School of Molecular Sciences, Arizona State University, Tempe, Arizona 85287, United States

Nour Eddine Fahmi — Center for Molecular Design and Biomimetics at the Biodesign Institute, and School of Molecular Sciences, Arizona State University, Tempe, Arizona 85287, United States

Huiyu Hu — Center for Molecular Design and Biomimetics at the Biodesign Institute, and School of Molecular Sciences, Arizona State University, Tempe, Arizona 85287, United States; orcid.org/0000-0002-6936-2398

Matthew Vrbanc — Center for Molecular Design and Biomimetics at the Biodesign Institute, and School of Molecular Sciences, Arizona State University, Tempe, Arizona 85287, United States

Complete contact information is available at: <https://pubs.acs.org/doi/10.1021/acsnano.1c00027>

Author Contributions

S.J., H.Y., and Y.L. designed the research. S.J., N.P., F.H., N.E.F., H.H., and M.V. performed the research. S.J., N.P., and F.H. analyzed the data. S.J., N.P., H.Y., N.G.W., and Y.L. wrote the manuscript. All authors have approved the final version of the manuscript.

Notes

The authors declare no competing financial interest.

ACKNOWLEDGMENTS

This work was supported by National Science Foundation grant 1607832.

REFERENCES

- (1) Whitesides, G. M.; Mathias, J. P.; Seto, C. T. Molecular Self-Assembly and Nanochemistry: A Chemical Strategy for the Synthesis of Nanostructures. *Science* **1991**, 254, 1312–1319.
- (2) Kelton, K. F. Crystal Nucleation in Liquids and Glasses. *Solid State Phys.* **1991**, 45, 75–177.
- (3) Fersht, A. R. Nucleation Mechanisms in Protein Folding. *Curr. Opin. Struct. Biol.* **1997**, 7, 3–9.
- (4) Whitesides, G. M.; Grzybowski, B. Self-Assembly at All Scales. *Science* **2002**, 295, 2418–2421.
- (5) Grzybowski, B. A.; Wilmer, C. E.; Kim, J.; Browne, K. P.; Bishop, K. J. M. Self-Assembly: From Crystals to Cells. *Soft Matter* **2009**, 5, 1110–1128.
- (6) Desai, A.; Mitchison, T. J. Microtubule Polymerization Dynamics. *Annu. Rev. Cell Dev. Biol.* **1997**, 13, 83–117.

- (7) Wittmann, T.; Hyman, A.; Desai, A. The Spindle: A Dynamic Assembly of Microtubules and Motors. *Nat. Cell Biol.* **2001**, *3*, E28–34.
- (8) Brouhard, G. J.; Rice, L. M. Microtubule Dynamics: An Interplay of Biochemistry and Mechanics. *Nat. Rev. Mol. Cell Biol.* **2018**, *19*, 451–463.
- (9) Kollman, J. M.; Merdes, A.; Mourey, L.; Agard, D. A. Microtubule Nucleation by Gamma-Tubulin Complexes. *Nat. Rev. Mol. Cell Biol.* **2011**, *12*, 709–721.
- (10) Roostalu, J.; Surrey, T. Microtubule Nucleation: Beyond the Template. *Nat. Rev. Mol. Cell Biol.* **2017**, *18*, 702–710.
- (11) Chen, Y. J.; Groves, B.; Muscat, R. A.; Seelig, G. DNA Nanotechnology from the Test Tube to the Cell. *Nat. Nanotechnol.* **2015**, *10*, 748–760.
- (12) Seeman, N. C.; Sleiman, H. F. DNA Nanotechnology. *Nat. Rev. Mater.* **2018**, *3*, 17068.
- (13) Li, J.; Green, A. A.; Yan, H.; Fan, C. Engineering Nucleic Acid Structures for Programmable Molecular Circuitry and Intracellular Biocomputation. *Nat. Chem.* **2017**, *9*, 1056–1067.
- (14) Bujold, K. E.; Lacroix, A.; Sleiman, H. F. DNA Nanostructures at the Interface with Biology. *Chem.* **2018**, *4*, 495–521.
- (15) Pinheiro, A. V.; Han, D.; Shih, W. M.; Yan, H. Challenges and Opportunities for Structural DNA Nanotechnology. *Nat. Nanotechnol.* **2011**, *6*, 763–772.
- (16) Zhang, F.; Nangreave, J.; Liu, Y.; Yan, H. Structural DNA Nanotechnology: State of the Art and Future Perspective. *J. Am. Chem. Soc.* **2014**, *136*, 11198–11211.
- (17) Zhang, D. Y.; Seelig, G. Dynamic DNA Nanotechnology Using Strand-Displacement Reactions. *Nat. Chem.* **2011**, *3*, 103–113.
- (18) Lin, C.; Liu, Y.; Rinker, S.; Yan, H. DNA Tile Based Self-Assembly: Building Complex Nanoarchitectures. *ChemPhysChem* **2006**, *7*, 1641–1647.
- (19) Winfree, E. *Algorithmic Self-Assembly of DNA*. Ph.D. Thesis, California Institute of Technology, Pasadena, CA, 1998.
- (20) Evans, C. G.; Winfree, E. Physical Principles for DNA Tile Self-Assembly. *Chem. Soc. Rev.* **2017**, *46*, 3808–3829.
- (21) Barish, R. D.; Rothmund, P. W.; Winfree, E. Two Computational Primitives for Algorithmic Self-Assembly: Copying and Counting. *Nano Lett.* **2005**, *5*, 2586–2592.
- (22) Schulman, R.; Winfree, E. Synthesis of Crystals with a Programmable Kinetic Barrier to Nucleation. *Proc. Natl. Acad. Sci. U. S. A.* **2007**, *104*, 15236–15241.
- (23) Zhang, D. Y.; Hariadi, R. F.; Choi, H. M.; Winfree, E. Integrating DNA Strand-Displacement Circuitry with DNA Tile Self-Assembly. *Nat. Commun.* **2013**, *4*, 1965.
- (24) Rothmund, P. W. Folding DNA to Create Nanoscale Shapes and Patterns. *Nature* **2006**, *440*, 297–302.
- (25) Fujibayashi, K.; Hariadi, R.; Park, S. H.; Winfree, E.; Murata, S. Toward Reliable Algorithmic Self-Assembly of DNA Tiles: A Fixed-Width Cellular Automaton Pattern. *Nano Lett.* **2008**, *8*, 1791–1797.
- (26) Barish, R. D.; Schulman, R.; Rothmund, P. W.; Winfree, E. An Information-Bearing Seed for Nucleating Algorithmic Self-Assembly. *Proc. Natl. Acad. Sci. U. S. A.* **2009**, *106*, 6054–6059.
- (27) Schulman, R.; Yurke, B.; Winfree, E. Robust Self-Replication of Combinatorial Information via Crystal Growth and Scission. *Proc. Natl. Acad. Sci. U. S. A.* **2012**, *109*, 6405–6410.
- (28) Mohammed, A. M.; Schulman, R. Directing Self-Assembly of DNA Nanotubes Using Programmable Seeds. *Nano Lett.* **2013**, *13*, 4006–4013.
- (29) Li, W.; Yang, Y.; Jiang, S.; Yan, H.; Liu, Y. Controlled Nucleation and Growth of DNA Tile Arrays within Prescribed DNA Origami Frames and Their Dynamics. *J. Am. Chem. Soc.* **2014**, *136*, 3724–3727.
- (30) Mohammed, A. M.; Sulc, P.; Zenk, J.; Schulman, R. Self-Assembling DNA Nanotubes to Connect Molecular Landmarks. *Nat. Nanotechnol.* **2017**, *12*, 312–316.
- (31) Jorgenson, T. D.; Mohammed, A. M.; Agrawal, D. K.; Schulman, R. Self-Assembly of Hierarchical DNA Nanotube Architectures with Well-Defined Geometries. *ACS Nano* **2017**, *11*, 1927–1936.
- (32) Green, L. N.; Subramanian, H. K. K.; Mardanlou, V.; Kim, J.; Hariadi, R. F.; Franco, E. Autonomous Dynamic Control of DNA Nanostructure Self-Assembly. *Nat. Chem.* **2019**, *11*, 510–520.
- (33) Pinheiro, A. V.; Nangreave, J.; Jiang, S.; Yan, H.; Liu, Y. Steric Crowding and the Kinetics of DNA Hybridization within a DNA Nanostructure System. *ACS Nano* **2012**, *6*, 5521–5530.
- (34) Rauzan, B.; McMichael, E.; Cave, R.; Sevcik, L. R.; Ostrosky, K.; Whitman, E.; Stegemann, R.; Sinclair, A. L.; Serra, M. J.; Deckert, A. A. Kinetics and Thermodynamics of DNA, RNA, and Hybrid Duplex Formation. *Biochemistry* **2013**, *52*, 765–772.
- (35) Jiang, S.; Yan, H.; Liu, Y. Kinetics of DNA Tile Dimerization. *ACS Nano* **2014**, *8*, 5826–5832.
- (36) Jiang, S.; Hong, F.; Hu, H.; Yan, H.; Liu, Y. Understanding the Elementary Steps in DNA Tile-Based Self-Assembly. *ACS Nano* **2017**, *11*, 9370–9381.
- (37) Schulman, R.; Winfree, E. Programmable Control of Nucleation for Algorithmic Self-Assembly. In *DNA Computing*; Ferretti, C., Mauri, G., Zandron, C., Eds.; Springer: Berlin, Heidelberg, 2005; Vol. 3384, pp 319–328.
- (38) Schulman, R.; Winfree, E. Programmable Control of Nucleation for Algorithmic Self-Assembly. *SIAM J. Comput.* **2010**, *39*, 1581–1616.
- (39) Fu, T. J.; Seeman, N. C. DNA Double-Crossover Molecules. *Biochemistry* **1993**, *32*, 3211–3220.
- (40) Torimura, M.; Kurata, S.; Yamada, K.; Yokomaku, T.; Kamagata, Y.; Kanagawa, T.; Kurane, R. Fluorescence-Quenching Phenomenon by Photoinduced Electron Transfer between a Fluorescent Dye and a Nucleotide Base. *Anal. Sci.* **2001**, *17*, 155–160.
- (41) Dose, S.; Neuweiler, H.; Sauer, M. Fluorescence Quenching by Photoinduced Electron Transfer: A Reporter for Conformational Dynamics of Macromolecules. *ChemPhysChem* **2009**, *10*, 1389–1398.
- (42) Rothmund, P. W.; Ekani-Nkodo, A.; Papadakis, N.; Kumar, A.; Fygenson, D. K.; Winfree, E. Design and Characterization of Programmable DNA Nanotubes. *J. Am. Chem. Soc.* **2004**, *126*, 16344–16352.
- (43) Fischer, S.; Hartl, C.; Frank, K.; Radler, J. O.; Liedl, T.; Nickel, B. Shape and Interhelical Spacing of DNA Origami Nanostructures Studied by Small-Angle X-Ray Scattering. *Nano Lett.* **2016**, *16*, 4282–4287.
- (44) Wagenbauer, K. F.; Wachauf, C. H.; Dietz, H. Quantifying Quality in DNA Self-Assembly. *Nat. Commun.* **2014**, *5*, 3691.
- (45) Myhrvold, C.; Baym, M.; Hanikel, N.; Ong, L. L.; Gootenberg, J. S.; Yin, P. Barcode Extension for Analysis and Reconstruction of Structures. *Nat. Commun.* **2017**, *8*, 14698.
- (46) Strauss, M. T.; Schueder, F.; Haas, D.; Nickels, P. C.; Jungmann, R. Quantifying Absolute Addressability in DNA Origami with Molecular Resolution. *Nat. Commun.* **2018**, *9*, 1600.
- (47) Evans, C. G.; Hariadi, R. F.; Winfree, E. Direct Atomic Force Microscopy Observation of DNA Tile Crystal Growth at the Single-Molecule Level. *J. Am. Chem. Soc.* **2012**, *134*, 10485–10492.
- (48) Rothmund, P. W.; Papadakis, N.; Winfree, E. Algorithmic Self-Assembly of DNA Sierpinski Triangles. *PLoS Biol.* **2004**, *2*, No. e424.
- (49) Chen, H. L.; Schulman, R.; Goel, A.; Winfree, E. Reducing Facet Nucleation During Algorithmic Self-Assembly. *Nano Lett.* **2007**, *7*, 2913–2919.
- (50) Gerling, T.; Wagenbauer, K. F.; Neuner, A. M.; Dietz, H. Dynamic DNA Devices and Assemblies Formed by Shape-Complementary, Non-Base Pairing 3D Components. *Science* **2015**, *347*, 1446–1452.
- (51) Bruetzel, L. K.; Walker, P. U.; Gerling, T.; Dietz, H.; Lipfert, J. Time-Resolved Small-Angle X-Ray Scattering Reveals Millisecond Transitions of a DNA Origami Switch. *Nano Lett.* **2018**, *18*, 2672–2676.
- (52) Bruetzel, L. K.; Gerling, T.; Sedlak, S. M.; Walker, P. U.; Zheng, W.; Dietz, H.; Lipfert, J. Conformational Changes and Flexibility of DNA Devices Observed by Small-Angle X-Ray Scattering. *Nano Lett.* **2016**, *16*, 4871–4879.
- (53) Wagenbauer, K. F.; Sigl, C.; Dietz, H. Gigadalton-Scale Shape-Programmable DNA Assemblies. *Nature* **2017**, *552*, 78–83.

(54) Erickson, H. P.; O'Brien, E. T. Microtubule Dynamic Instability and GTP Hydrolysis. *Annu. Rev. Biophys. Biomol. Struct.* **1992**, *21*, 145–166.

(55) Fu, J.; Yang, Y. R.; Johnson-Buck, A.; Liu, M.; Liu, Y.; Walter, N. G.; Woodbury, N. W.; Yan, H. Multi-Enzyme Complexes on DNA Scaffolds Capable of Substrate Channelling with an Artificial Swinging Arm. *Nat. Nanotechnol.* **2014**, *9*, 531–536.

(56) Michelotti, N.; de Silva, C.; Johnson-Buck, A. E.; Manzo, A. J.; Walter, N. G. A Bird's Eye View Tracking Slow Nanometer-Scale Movements of Single Molecular Nano-Assemblies. *Methods Enzymol.* **2010**, *475*, 121–148.

(57) Tsekouras, K.; Custer, T. C.; Jashnsaz, H.; Walter, N. G.; Presse, S. A Novel Method to Accurately Locate and Count Large Numbers of Steps by Photobleaching. *Mol. Biol. Cell* **2016**, *27*, 3601–3615.

Supporting Information

Regulating DNA Self-Assembly Dynamics with Controlled Nucleation

Shuoxing Jiang¹, Nibedita Pal^{2,†}, Fan Hong¹, Nour Eddine Fahmi¹, Huiyu Hu¹, Matthew Vrbanc¹,
Hao Yan^{1,*}, Nils G. Walter^{2,*}, Yan Liu^{1,*}

¹Center for Molecular Design and Biomimetics at the Biodesign Institute, and School of Molecular Sciences, Arizona State University, Tempe, AZ 85287, USA

²Single Molecule Analysis Group, Department of Chemistry, University of Michigan, Ann Arbor, MI 48109, USA

[†]Present address: Indian Institute of Science Education and Research (IISER) Tirupati, Tirupati 517507, Andhra Pradesh, India

Content

	Page
S1. Data Analysis	S3
S2. Design of the DNA Origami Frame	S8
S3. Kinetic Simulation by Ordinary Differential Equation (ODE) Model	S9
S4. Additional AFM Images and Yield Quantification	S11
S5. Stepwise Photobleaching Counting of Single-Fluorophore Labeled Tiles	S14
S6. Sequences	S15

S1 Data Analysis

S1.1 Thermal curves of the tile lattice: concentration dependence of T_m

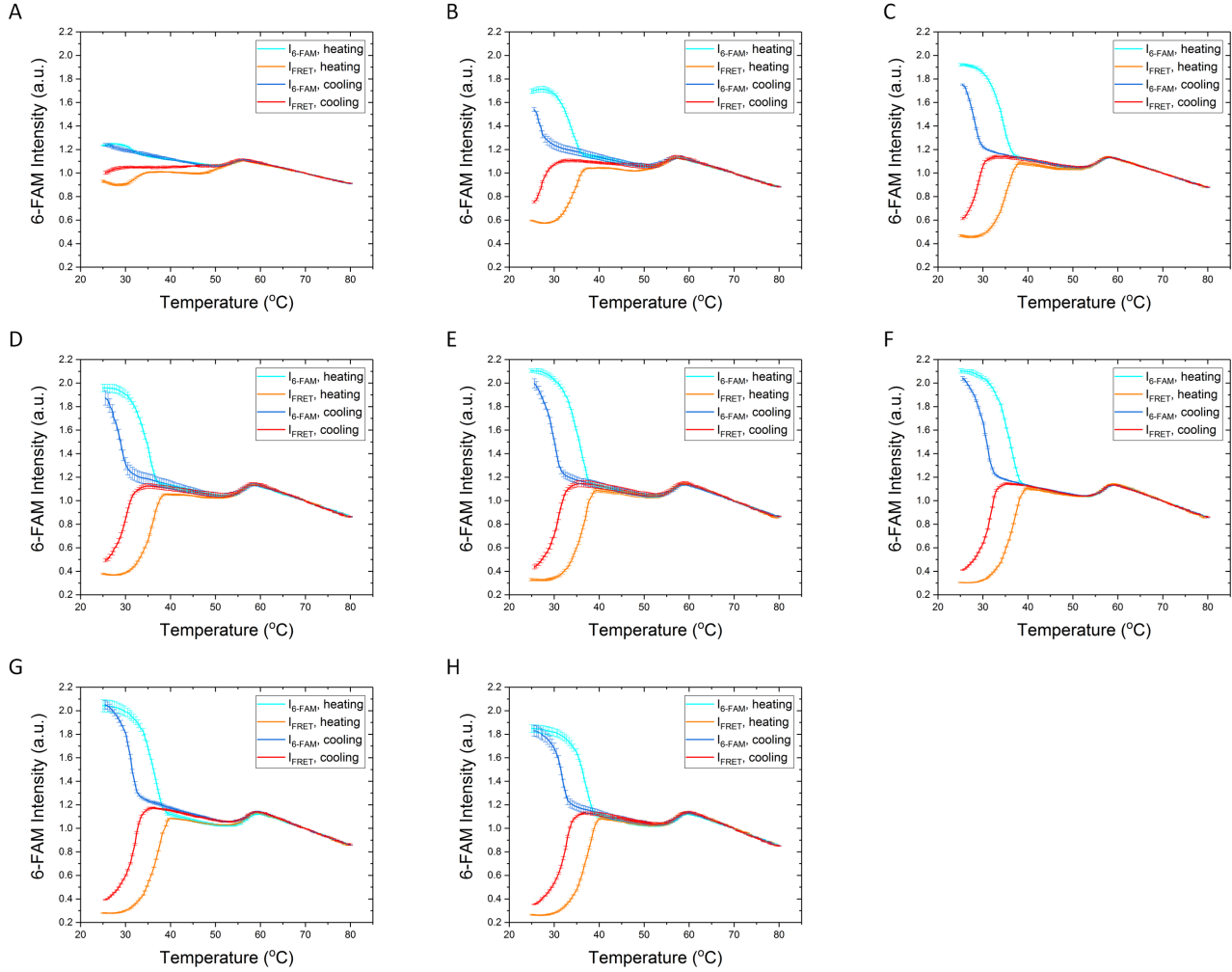


Figure S1. The cooling and heating curves (6-FAM fluorescence intensity vs. temperature) of the self-complementary tile lattices at different monomer tile concentrations. Tile concentrations are (A) 100 nM; (B) 200 nM; (C) 300 nM; (D) 400 nM; (E) 500 nM; (F) 600 nM; (G) 700 nM; (H) 800 nM. The transition at 50-60°C corresponds to the tile formation (*i.e.*, complete incorporation of the 6-FAM modified strand into the tile); the transition below 45°C corresponds to the growth of the lattice (*i.e.*, inter-tile binding through sticky end hybridization). I_{6-FAM} : 6-FAM intensity of the donor-only sample, I_{FRET} , 6-FAM intensity of the donor-acceptor dual labeled sample.

The fluorescence intensity difference of 6-FAM (ΔI) between the donor only (I_{6-FAM}) and donor/acceptor (I_{FRET}) samples at each temperature was calculated by the following equation:

$$\Delta I = I_{6-FAM} - I_{FRET} \quad (1)$$

where I_{6-FAM} and I_{FRET} are the fluorescence intensities of the donor 6-FAM in the absence and presence of the acceptor, respectively. ΔI was assumed to be proportional to the concentration of bound tiles. At each temperature, the growth of tiles onto the lattice reached equilibrium because of the slow temperature gradient. The melting temperature was then obtained by fitting the first derivative of ΔI vs. temperature with a Gaussian function:

$$f(T | T_m, w^2) = Y_0 + \frac{A}{w\sqrt{\pi/2}} e^{-2\left(\frac{T-T_m}{w}\right)^2} \quad (2)$$

where T_m is the midpoint of transition temperature and w represents the width of the transition, which is ~ 0.849 of the full width of the peak at half maximum (FWHM). The concentration dependence of T_m was analyzed by the following equation, which assumes a two-state model,¹ to obtain standard enthalpy (ΔH°) and entropy (ΔS°) change for single tile attachment:

$$\frac{1}{T_m} = \frac{R \ln(C_0 / 2)}{\Delta H^\circ} + \frac{\Delta S^\circ}{\Delta H^\circ} \quad (3)$$

Table S1. Experimentally measured T_m of the tile lattice that increases with the tile concentration.

Concentration (nM)	T_m (°C)
100	31.9±0.1
200	33.8±0.1
300	34.4±0.1
400	35.0±0.1
500	35.6±0.1
600	35.8±0.1
700	36.3±0.1
800	36.8±0.1

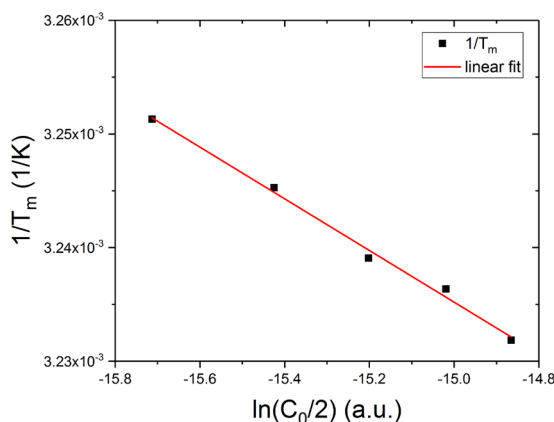


Figure S2. Linear fitting of the concentration-dependent T_m gives the standard enthalpy change ($\Delta H^\circ = -87.4 \pm 5.3$ kcal/mol), entropy change ($\Delta S^\circ = -0.252 \pm 0.015$ kcal/mol). Thus, the standard free energy change (ΔG°) for the attachment of a monomer tile can be calculated as -12.1 kcal/mol at 298 K. Data points for 300-700 nM were used for this plot. Data points for 100 and 200 nM were excluded due to the relatively weak transitions, and data point for 800 nM was not used due to detector signal saturation

Note: The thermodynamic parameters obtained here agree well with the values obtained from a previous study on the elementary steps in DNA tile-based self-assembly,⁵ which gives ΔH° ranging from -85.2 to -95.1 kcal/mol, ΔS° ranging from -0.244 to -0.271 kcal/mol, and ΔG° ranging from -12.3 to -14.3 kcal/mol for bivalent tile attachment mediated by two sticky ends, 5-nt each. The small changes in thermodynamic parameters result from the weaker sticky ends (40% GC content) used in this study. The thermodynamic parameters are subsequently used to parameterize the kinetic model to predict the competition between different nucleation modes in this study.

S1.2 Thermal curves of the tile lattice: $[Mg^{2+}]$ dependence of T_f

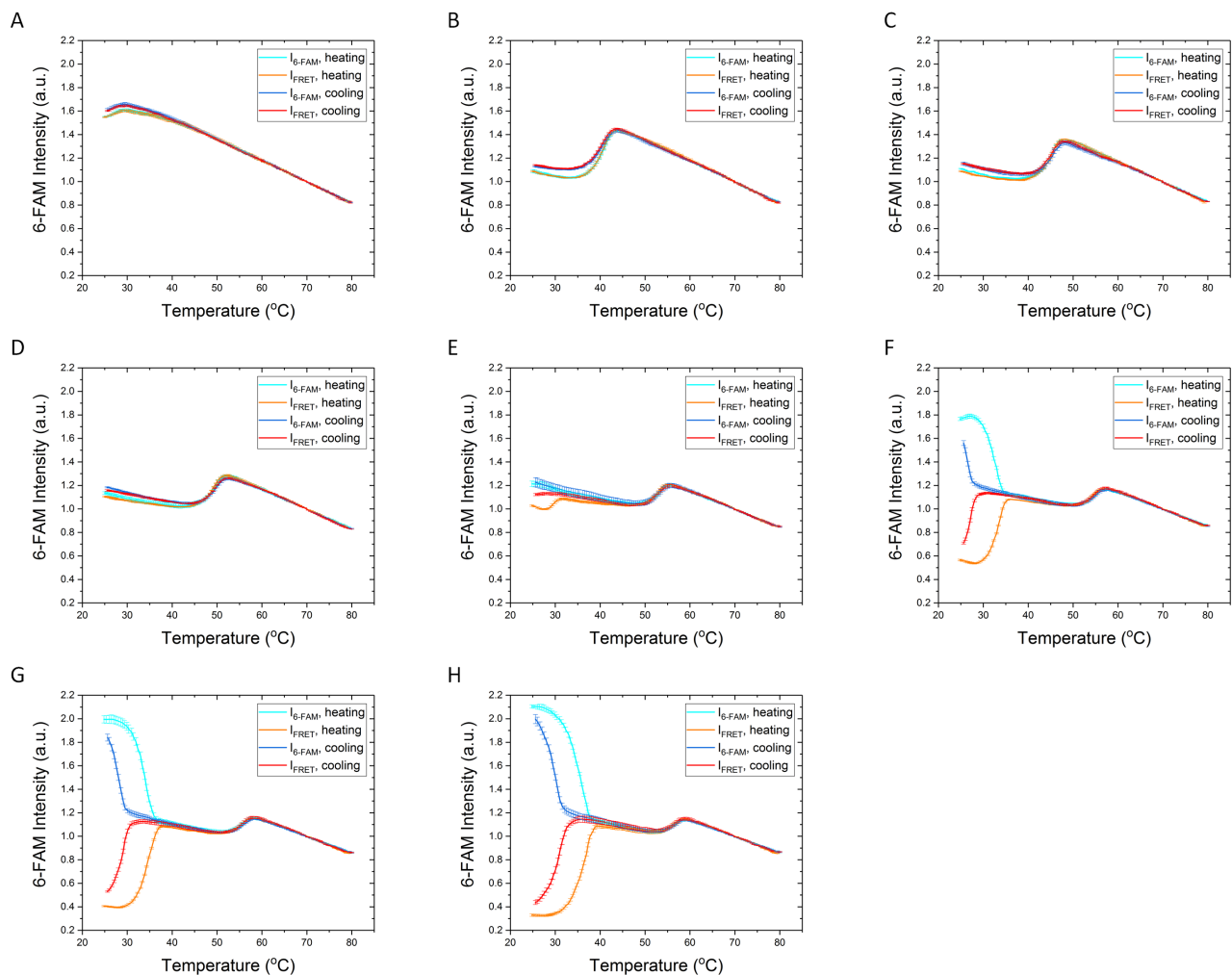


Figure S3. The cooling and heating curves (6-FAM fluorescence intensity vs. temperature) of the self-complementary tile lattices in $1\times$ TAE buffer containing different $[Mg^{2+}]$. (A) 2.0 mM; (B) 2.5 mM; (C) 3.0 mM; (D) 4.0 mM; (E) 6.0 mM; (F) 8.0 mM; (G) 10.0 mM; (H) 12.5 mM. As $[Mg^{2+}]$ decreases, both transitions of tile formation and tile growth shift to lower temperature regions. The transition of lattice growth no longer exists above 25°C when $[Mg^{2+}]$ is below 3.0 mM, showing overlapping I_{6-FAM} and I_{FRET} curves for both heating (cyan and orange) and cooling (blue and red) cycles. Thus, 2.5 mM $[Mg^{2+}]$ was used to prepare monomer tile solution at room temperature. Considering the chelation ability of 2.0 mM EDTA in the buffer recipe, the effective $[Mg^{2+}]$ is ~ 0.5 mM to maintain a stable monomeric tile at room temperature.

S1.3 Stability of the monomer tile

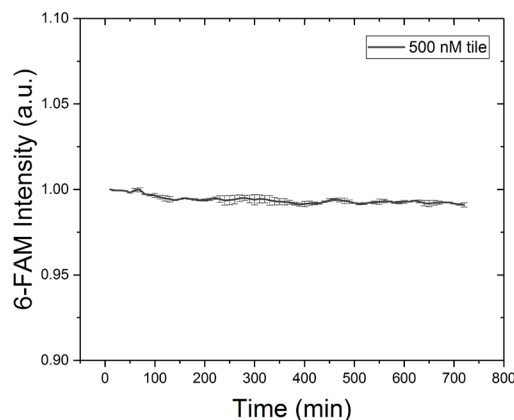


Figure S4. Stability test of the 500 nM monomer tile in 1×TAE buffer containing 2.5 mM Mg^{2+} at 26°C. The 6-FAM intensity remains stable over 12 hours except for a 1% signal decrease due to photobleaching of the 6-FAM reporter. Hence, the 500 nM monomer tile stock was held at 26°C to prevent spontaneous nucleation during the lengthy kinetic measurements.

S1.4 Thermal curves of seeded and facet nucleation

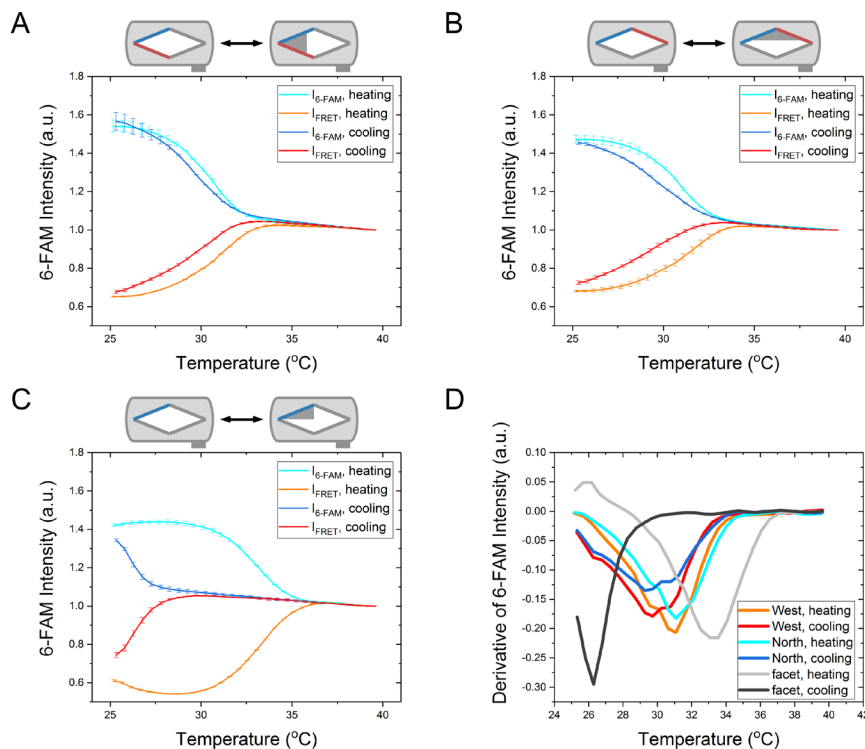


Figure S5. The cooling and heating curves (6-FAM intensity vs. temperature) of 100 nM self-complementary tile lattices in the presence of 4 nM nucleation seeds that present various growth frontiers measured from 25–40°C. (A) West frame presenting a bivalent binding site at the West corner; (B) North frame presenting a bivalent binding site at the North corner; (C) facet frame presenting monovalent binding sites along the NW edge. (D) The first derivative of the cooling and heating transition of the seeded and facet nucleation. The transition along the cooling curve represents the formation of the tile lattice (the midpoint of the transition is T_f), while the transition along the heating

curve represents the dissociation of tiles from the tile lattice (the midpoint of the transition is T_m). Comparing to unseeded nucleation of the same tile concentration (100 nM, Figure S1A) that only shows an incomplete growth transition down to 25°C, the presence of a bivalent seed significantly increases the T_f to ~30°C. The nucleation seed with a bivalent binding site facilitates nucleation more effectively than the facet frame with only monovalent binding sites, resulting in a ~4°C difference in the lattice formation temperature. In all cases, a hysteresis between the heating and cooling curves was observed. The presence of West or North frame reduces the hysteresis between the T_f and T_m to ~2°C, but cannot eliminate it.

S1.5 Kinetic curve normalization

The original fluorescent curves were processed by applying photobleaching correction and normalization to reflect the fractional yield of tile attachment. Although the protocol for kinetic measurement was optimized to minimize the effect of photobleaching, the 1800 s excitation time still results in ~2.5% reduction in the fluorescence intensity of the reporter fluorophore, 6-FAM (Figure S6). The effect of photobleaching was quantified by monitoring unseeded nucleation at 26°C, which is high enough to inhibit unseeded nucleation of 20 nM tiles. Then, the fluorescent curve was normalized to the initial fluorescent intensity at time 0 (I_0) and fitted by a linear function, which serves as the correction function for photobleaching. The normalization and correction were applied to all the other kinetic curves. To obtain the yield of tile attachment, the kinetic curves were normalized by the theoretical percentage of fluorescence enhancement when all the tiles are consumed by self-assembly. 40% fluorescence enhancement was adapted from the elementary tile attachment study² and applied to the normalization.

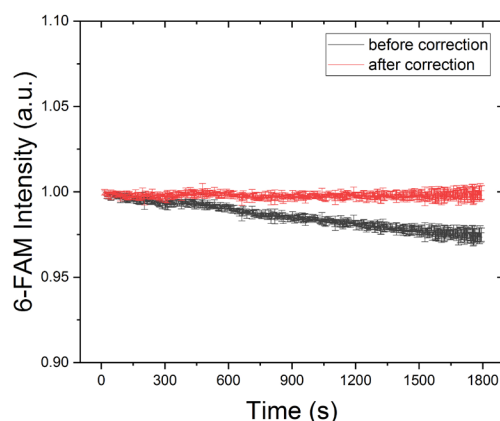


Figure S6. The baseline for photobleaching correction. The baseline was obtained by monitoring the kinetic curves of unseeded nucleation at 26°C, which was high enough to inhibit unseeded nucleation in solution. Photobleaching resulted in ~2.5 % reduction in the fluorescence intensity for the averaged kinetic curve of triplicate measurements. Fitting the kinetic curve with a linear function gave the slope of photobleaching as $-(1.394 \pm 0.009) \times 10^{-5} \text{ s}^{-1}$, which was used to correct photobleaching for all the kinetic curves.

S2 Design of the DNA Origami Frame

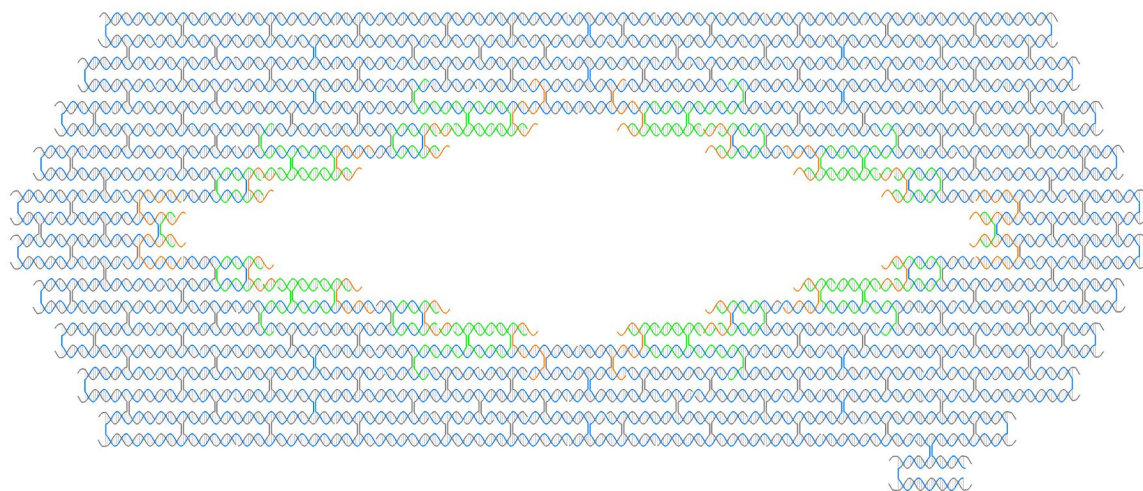


Figure S7. Detailed design of the DNA origami frame for kinetic measurements. The blue strand represents the M13mp18 scaffold. The interior edge is composed of staple strands carrying the sticky ends (orange) and the other staple strands holding the sticky ends in position (green). The rest of the staple strands (gray) fold the scaffold into the frame. The staple strands on the outer edges are extended by three thymine bases on both ends to avoid π - π stacking between origami frames. Sequences of the staple strands are listed in Table S6-8.

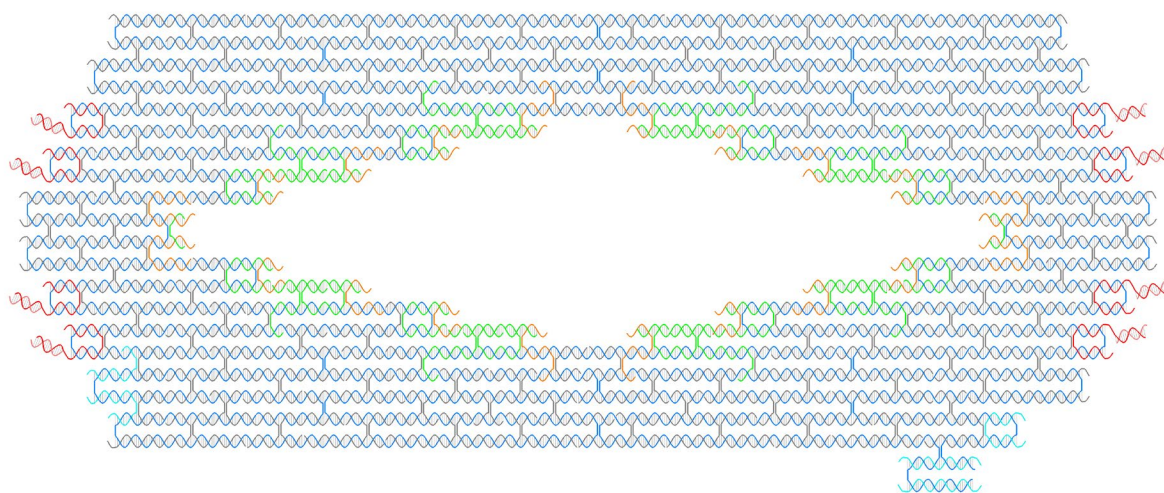


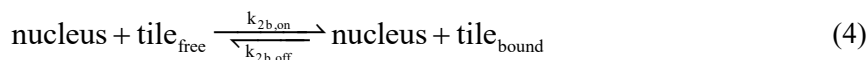
Figure S8. Detailed design of the DNA origami frame for single-molecule tile counting. The blue strand represents the M13mp18 scaffold. The interior edge is composed of staple strands carrying the sticky ends (orange) and staple strands holding the sticky ends in position (green). Eight positions (red) are extended for hybridizing with Atto647 labeled strand (pink) as the fluorescent marker. Five staple strands (cyan) are labeled with biotin for immobilization on the streptavidin-modified substrate surface. The rest of the staple strands (gray) fold the scaffold into the frame. The staple strands on the outer edges are extended by three thymine bases on both ends to avoid π - π stacking between origami frames. Sequences of the staple strands are listed in Table S6-9.

S3 Kinetic Simulation by Ordinary Differential Equation (ODE) Model

S3.1 Assumptions

The reversibility of the reaction depends on the number of sticky ends involved (for the same length and strength of the sticky ends). Tile attached by one bond is more likely to dissociate than the tile attached by two bonds under the experimental conditions in this study. To predict the competition between the three nucleation modes, we made the following assumptions:

1. The formation of a complex in which every tile is attached by two bonds is considered successful nucleation, after which the assembly proceeds into the growth stage.
2. The difference between the three modes of nucleation is the number of 1-bond attachment steps required to form a critical nucleus.
3. In the growth stage, the nucleus can transform free tile(s) to bound tile(s) by 2-bond attachment and grow larger.



4. No matter how large the lattice is, the thermodynamic and kinetic properties of an attached tile are exclusively determined by the number of sticky ends that are involved.

5. The joining or splitting of existing lattices are not considered contributors to lattice growth or dissociation in this model.

S3.2 Thermodynamic and kinetic parameter initialization

For the tile used in this study, the bivalent attachment (2-bond) thermodynamics was measured by the tile concentration-dependent melting curve. A loop penalty ($\Delta G_{\text{Loop4}}^\circ$) is defined as the energy penalty to attach a tile through 2 bonds.² $\Delta G_{\text{Loop4}}^\circ$ is defined as +3.0 kcal/mol. The free energy change for 1-bond attachment is calculated from 2-bond attachment as follows:

$$\Delta G_{1b}^\circ = (\Delta G_{2b}^\circ - \Delta G_{\text{Loop4}}^\circ) / 2 \quad (5)$$

The rate constant of 2-bond attachment had been acquired from a previous study of single tile attachment.² The rate constant of 1-bond attachment was assumed to be equal to 2-bond attachment according to the assumption of kinetic tile assembly model (kTAM).³⁻⁵

Table S2. Thermodynamic and kinetic parameters used for the ODE modeling.

Number of bonds	ΔH° (kcal/mol)	ΔS° (kcal/mol)	$\ln(A \cdot M \cdot s)$	E_a (kcal/mol)
1	/	/	26.7	7.6
2	-87.4	-0.252	26.7	7.6

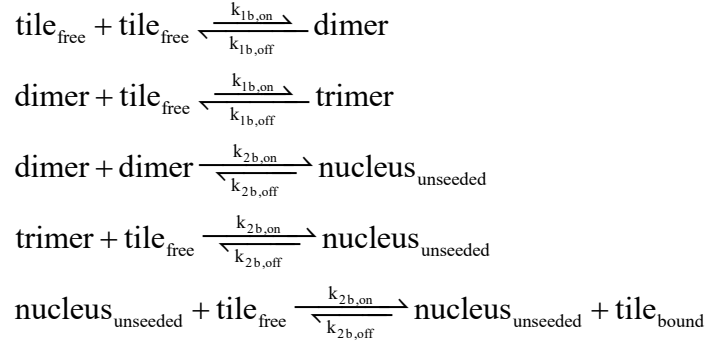
S3.3 ODE set.

Table S3. Species selected for the ODE model.

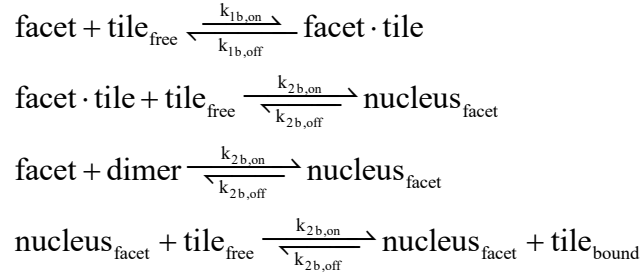
Starting materials	Intermediates	Products
tile _{free}	dimer	tile _{bound} (unseeded)
	trimer	
	unseeded nucleus	
facet	facet·tile	tile _{bound} (facet)
	facet nucleus	
seed	/	tile _{bound} (seeded)

A set of initial, intermediate, and product species (Table S3) are selected to depict the possible elementary reactions in the experimental system. The initial concentrations of the starting materials, including free monomer tile, facet, and seed, were initialized as 20.0, 6.4, and 0.8 nM, respectively. The interconversion between the above-mentioned species can be described by the following elementary reactions:

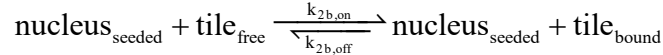
1. Unseeded nucleation and growth. Longer arrows indicate the thermodynamically preferred direction of the reaction under the modeling conditions.



2. Facet nucleation and growth.



3. Seeded nucleation and growth.



Some species such as $\text{tile}_{\text{free}}$ and dimer are shared among the three nucleation modes. Thus, different nucleation types compete and inhibit each other through the consumption of these mutual species. The corresponding ordinary differential equations are simulated using MATLAB's stiff "ode23s" solver under conditions mimicking the experimental conditions.

S4 Additional AFM Images and Yield Quantification

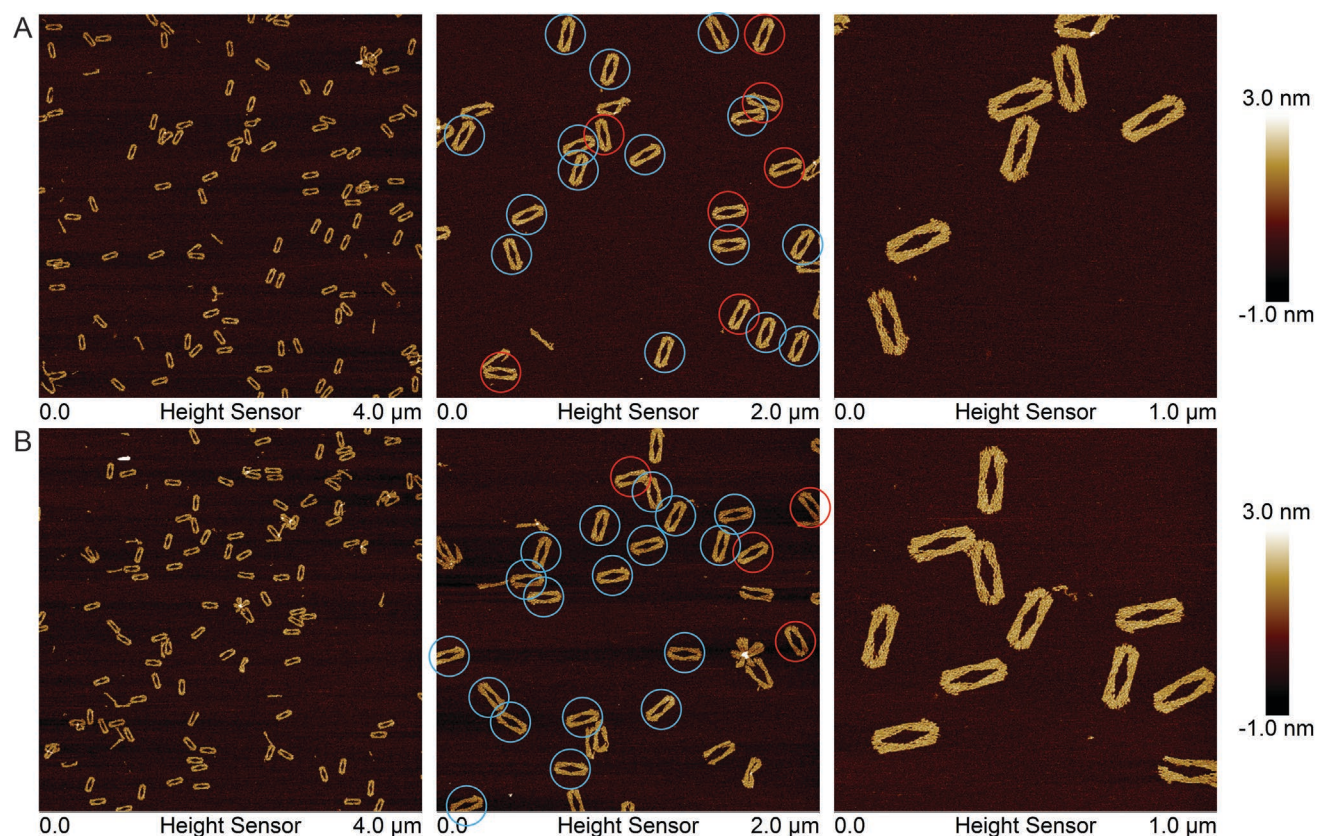


Figure S9. AFM characterization of the empty DNA origami frame. Scan size reduces from left to right. (A) West frame; (B) North frame. Monomeric origami frames were evenly distributed on the AFM substrate, suggesting the mono-dispersity of frames in solution. Some malformed origami frames were observed, which were majorly caused by the nicking of the M13mp18 scaffold strand. The malformed origami reduced the effective concentration of the frame. The asymmetric marker labeled at the bottom right of the origami frame allowed us to tell the direction of the origami frame landing on the substrate. Origami frames adopting face-up and face-down orientations were marked with red and blue circles, respectively. For the West frame, the ratio between face-up and face-down orientations is 7:15. For the North frame, the ratio is 4:18. The majority of the empty origami frames adopted the face-down orientation when depositing onto the mica surface (blue circle), suggesting that the curvature of the origami frame was in agreement with the curvature of the DAE-E tile used in this study.⁶

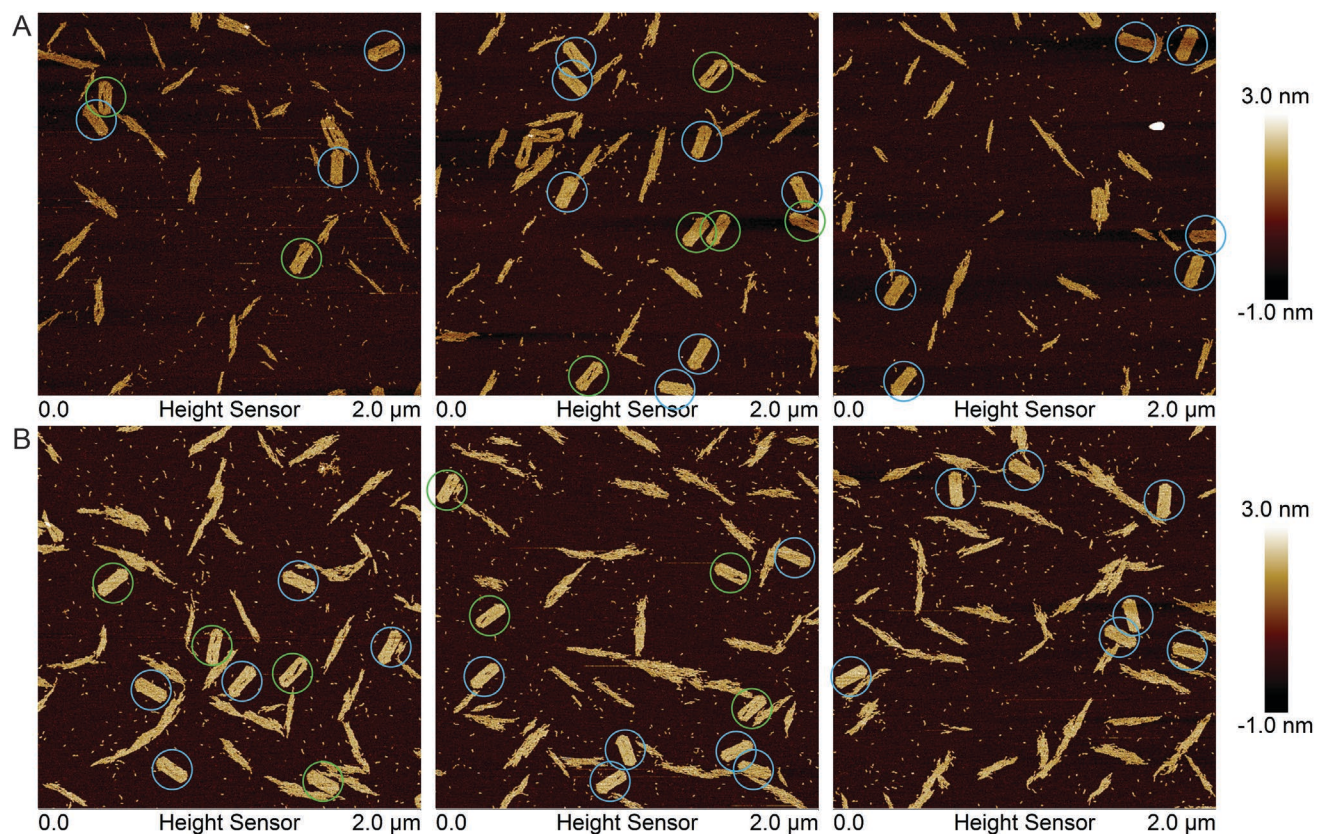


Figure S10. AFM characterization of the DNA origami frame filled by 2-fold DNA tiles (molar concentration ratio of the origami frame: tile = 1:50) at 22°C for 1 hr. (A) West frame. (B) North frame. Three non-overlapping scanning areas were shown for each sample. Partially filled and fully-filled frames were marked with green and blue circles, respectively. The majority of the well-formed frames were filled with > 90% yield with maximum 3 tiles missing. The missing tiles could be attributed to the reduced accessibility of the growth frontier when the growth was approaching the boundary of the template. Kinetic measurement suggested that 22°C did not favor unseeded nucleation in solution. However, mica substrate greatly promoted the heterogeneous nucleation of free tiles on its surface during 2 min sample preparation.⁷ The lattice growth outside of the frame was mainly due to substrate surface-mediated nucleation during imaging.

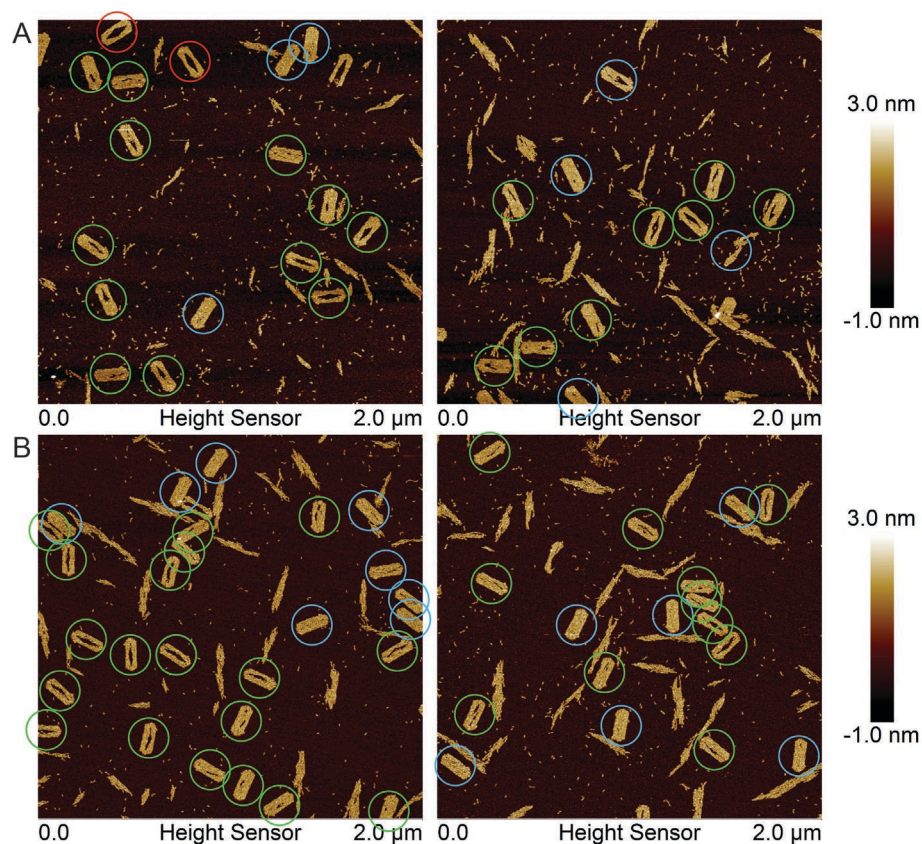


Figure S11. AFM characterization of the DNA origami frame filled by 1-fold DNA tiles (molar concentration ratio of the origami frame: tile = 1:25) at 22°C for 1 hr. (A) West frame. (B) North frame. Two different scanning areas were shown for each sample. Empty, partially filled, and fully-filled frames were marked with red, green, and blue circles, respectively. The average filling yield was approximately 60% for both frame designs. Again, the tile lattices outside the frame were mainly attributed to surface-mediated nucleation and growth during imaging.

S5 Stepwise Photobleaching Counting of Single-Fluorophore Labeled Tiles

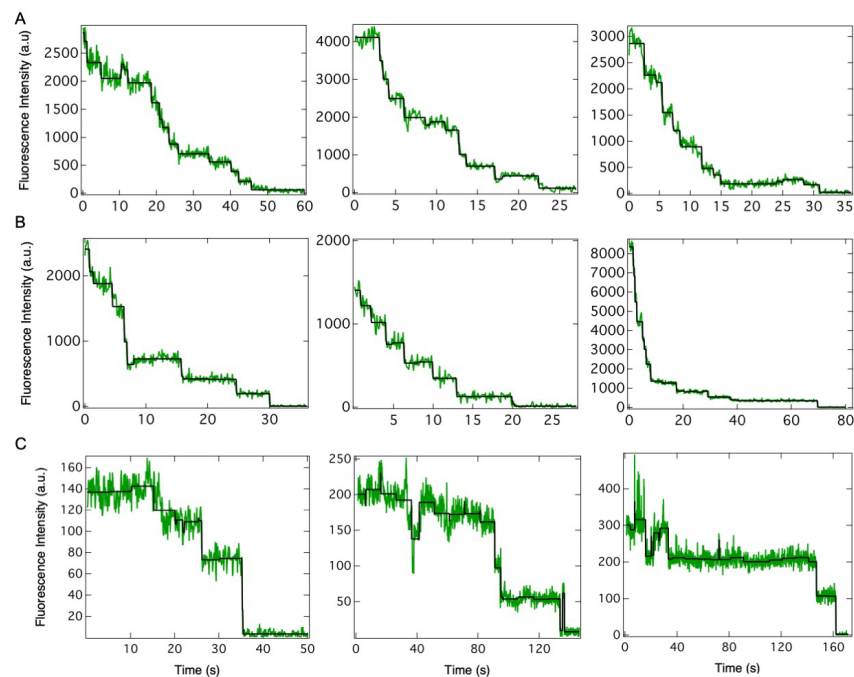


Figure S12. Representative single-tile stepwise photobleaching trajectories (green) of seeded W- (A), N- (B), and facet (C) frames with respective detected steps (black).

Table S4. Quantitative analysis of single-tile stepwise photobleaching experiment.

Frame	Number of origami frame investigated	Average number of tiles nucleated in a frame	Maximum number of tiles nucleated in a frame	Minimum number of tiles nucleated in a frame
W	70	13 ± 7	32	4
N	72	12 ± 6	32	5
facet	10	4 ± 2	8	2

[#] The error bars are given as the standard deviation of all the data.

S6 Sequence

Table S5. Sequences of the oligos composing the DNA tile.

Name	Sequence
tile-1	CTAGATCCTGACAATACAACCGCCATTCCTGAGACGA
tile-1-3'FAM	CTAGATCCTGACAATACAACCGCCATTCCTGAGACGA/36-FAM/
tile-2	TCAGTTCGTCTCACCGTAACCAGGTA
tile-3	TGTATTGTCACCGACAGCAGGTCCAGGCAGTGAATGGCGGT
tile-3-5'Cy3	/5Cy3/TGTATTGTCACCGACAGCAGGTCCAGGCAGTGAATGGCGGT
tile-4	ACTGAGTCGGAGTGGATCTAGTACCT
tile-4-5'TMR	/56-TAMN/ACTGAGTCGGAGTGGATCTAGTACCT
tile-5	GGTTACGGACTGCCTGGACCTGCTGTCGGACTCCGAC

Table S6. Sequences of the staple strands (gray-colored in Figure S7) composing the DNA origami frame.

Name	Sequence
Frame4Turn_core2	ATTAACCGTTGTAGGCCGATTAAAGGGATTTAGACAGGGCTAGGGCGCTGG
Frame4Turn_core3	CAAGTGTAGCGGTTTAGAGCTTGACGGGGAAAGCCGGCGTCCACTATTAAAG
Frame4Turn_core4	CCCCGATCACGCTGCGCGTAACCCGGGAGCT
Frame4Turn_core5	AGAACTCAAGCACGTATAACGTGCTTTCCTCGTTAGAATCAGAGACCACACC
Frame4Turn_core6	CGCCGCGCTTAATGCGCCGCCGTAAAGCACTAAATC
Frame4Turn_core7	GGGGTCGAGGTGCTACAGGGCGGCTACTATGGACTGTTGGGA
Frame4Turn_core8	AGGGCGATCGGCAATTCCACACAACATACGAGCAAGTTTTT
Frame4Turn_core9	GAAATTGTTATCCGCTCATGCGGGCCTCTTC
Frame4Turn_core10	GCTATTACGCCAGTGGTGCCGAAACCAGGC
Frame4Turn_core11	AGGGGGATCATGGTCATAGCTGTTCTCACATT
Frame4Turn_core12	CTGCCCCGAGCTCGAATTCGTAATGTGCTGCAAGGCGATT
Frame4Turn_core13	AAGTTGGGTAACGCCGATCCCCGGGTACCGTTTCCAG
Frame4Turn_core14	GCCAGCTGCAGGTCGACTCTAGAGAGGGTTTT
Frame4Turn_core15	GCATCTGCCAGTTTGACGACGTTGTAAAA
Frame4Turn_core16	CGACGGCCAGCAAATATTTGGCGCATCGTAACCGT
Frame4Turn_core17	CGGAGAGGGAACGGTAATCGTAAACTAGCATGTAAATCAG
Frame4Turn_core18	AACCCGTCTTAACCAATAGGAACGCCATCAAAAAAAAAACAAGA
Frame4Turn_core19	GAGTCTGGAGCTAATTCGCGTCTGGCCTTCCTTATCGCGTTT
Frame4Turn_core20	TAATTCGAGCTTCCATATAACAGTTGATTCCCCATTGCCTGA
Frame4Turn_core21	GGTGTCTGGAAGTTTCATTCAAAGCGAACCAGACCG
Frame4Turn_core22	GAAGCAAAAGCGGATTGCATCAAAAAGATTAAGAGGAAGCCGAATTTTGCAA
Frame4Turn_core23	AGAAGCAACTCCAACAGGTCAGGAGTTTTAAA
Frame4Turn_core24	TTTGATGGCTTAGAGCTTAATTGCTGAATATAATGCTGTAGCTCAACATTTAGAGAG
Frame4Turn_core25	TACCTTTAATTGCTCCTTCAAAAATCAGGTCTTTACCCTGACTATAGCGTCC
Frame4Turn_core26	CCATAAATTTGATAAGAGGTCATTTTTGCTTT
Frame4Turn_core28	ATCGGCAAAATCCCTTATAAATCAAAACGTCAAAGGGCGAAAAAAGGGAG

Frame4Turn_core29	GGAACCCCTAACCGTCTATCAGGGCGATGGCCCACTGATGGTGGTTCCGAA
Frame4Turn_core30	TTGCAGCACCTGGGGTGCCTAATGAGTGAGCTAATCCTGTGT
Frame4Turn_core31	TTGCATGCCTGCATTAATGAATCGGCCAACGCAAAGGGTG
Frame4Turn_core32	AAACGTTAAGCCCCAAAAACAGGAAGATTGTATAAGTGCCAAGC
Frame4Turn_core33	ATCAGAAAAATATTTTGTTAAAATTCGCATTAAATTTTGTCAATCATA
Frame4Turn_core34	CAATGCCTGAGTAATGCGGAGACAGTCAAATCACCATCAATAGGTTGATA
Frame4Turn_core35	TGTACCCCTGATATTCAACCGTTCTTTAGAACCCCTCATATATTTTAAATG
Frame4Turn_core36	GAATCGATGTAGCTATTTTGTAGATTTTGCGGGAGAAGCC
Frame4Turn_core37	CCTCAGAGCATAATAGTTTGACCATTAGATACATTTCGCTAAAGTAC
Frame4Turn_core38	TATGCAACAAATGGTCAATAACCTGAAAAGGTGGCATCAATTCTACAATAAAG
Frame4Turn_core39	AACGTGGACTCCAAGAATAGCCCGAGATAGGGTTGAGTGTGTTCCAGTTTTT
Frame4Turn_core40	AAAATCCTGTTTACGTGAACCATCACCCAAATCCGGAAGCAT
Frame4Turn_core41	AAAGTGTAAGAGCGGTCCACGCTGGTTTGCCCCAGCAGGCG
Frame4Turn_core42	AATTGCGTGCTGATTGCCCTTCACCGCCTGGCCCTGAGAGAG
Frame4Turn_core43	TCGGGAAAGTTTTCTTTTCACCAAGTGAGACGGGCAACATGCGCTCA
Frame4Turn_core44	GCGGTTTGCGTATTGGGCGCCAGGGTGCCTGTCGT
Frame4Turn_core45	AGAAAGGCTGTAGGTAAAGATTCAGCGGGGAGAG
Frame4Turn_core46	TTTATTTCAACGCAAGGATAAAAAATTTAGCTGATAAATTAATGC
Frame4Turn_core47	CCCTGTAATACGATCTACAAAGGCTATCAGGTAATTCTGCGA
Frame4Turn_core48	ACGAGTAGATTAGCTAAATCGGTTGTACCAAAAACATTATGA
Frame4Turn_core49	TTTTAATTCTGTCCAGACGACGACAATAAACACATGTTTCGTAATAAGAGAAT
Frame4Turn_core50	ATATGCGTAGGCATTTTCGAGCCAAGCTAATGCAGAACGCGCCTGTTTAT
Frame4Turn_core51	CAACAATAGATAAGTCACAACGCCAACATGTAATTTAGGCAGTATACAAA
Frame4Turn_core52	CGCCATATTTACTGAACAAGAAAAATAATATCCCATCCTAAT
Frame4Turn_core53	TTACGAGCATGCTTAAATCAAGATTAGTTGCTAATTGAGAAT
Frame4Turn_core54	ACGCTAACTCCCGACTTGCGGGAGGTTTTGAAGCTAGAAACC
Frame4Turn_core55	AATCAATAATCGGCTGTCTTTCCTTATCATTCCAGGCGTTTT
Frame4Turn_core56	GAACGCGAAGAACGGGTATTAACCAAGTACCGCACTCAAGAAGGCT
Frame4Turn_core57	TCAGATATTCGAGAACAAGCAAGCCGTTTTTATTT
Frame4Turn_core58	TCATCGTAGGCATAATCAAAATCACCGCGTTTGC
Frame4Turn_core59	CCGACTTGCATTTTCGGTCATAGCCCCCTTATTAGGAACCAGAGCCACCA
Frame4Turn_core60	CCGGAACCGCCTCCCTCAGAGCCGCCAGCGCGTTTTTCATCGGAGCCATTT
Frame4Turn_core61	CCTTTAGCGTCAGACTGTACCCTCAGAACCGCCACCCTCAGAGC
Frame4Turn_core62	CACCACCCTCAGAGCCTCAGTAGCGACAGAATATTACCAT
Frame4Turn_core63	CAGCACCGTAAGCCACCAGAACCACCACCAGAGCCGCCGCCA
Frame4Turn_core64	GCATTGACAGGGGTCAAGTGCCTTGAGTAACAGCCATCGATAG
Frame4Turn_core65	ACCTATTAAGTGTACTGGTAATAAGTTTTAACGGAGGTTGAGGCAGGTCA
Frame4Turn_core66	GACGATTGGCCTTGATATTCACAAACCTTTTGATGATACAGGTTCTGAAA
Frame4Turn_core67	GCGTCATACATGGAAATAAATCCTCATTAAAGCCAGAATGGAAAGCGCAGTTT
Frame4Turn_core68	TTTTTAAATAAGAATAAACACCGGAAAAGGTAAAGTTT

Frame4Turn_core69	ATAAAGTACCGACAATCATAATTACTAGAAAAAGCCTGTACCTAAATTTAAT
Frame4Turn_core70	AGCGAACCGAGCGTCTTTCCAGAGGACGGGAG
Frame4Turn_core71	CAGGGAAGCGCATTACCTAATTTGCCAGTTATATTCTAA
Frame4Turn_core72	TATCCGGCAAAATAAACAGCCAGAGAATAACATAAAAA
Frame4Turn_core73	TTTACAGATATTATTTATCCCAATCAAGCAA
Frame4Turn_core74	CATCTTTTAATCATTACCGCGCCAATAGCCAAATAAGAA
Frame4Turn_core75	TTTACCAGGAGCCAGCAAAATCACCAGTAGCACCCAAGTTTG
Frame4Turn_core76	GAGGGTTGATATATATTAAGAGGCTGAGACTCCTCAAGAACCGTTCCAGTAA
Frame4Turn_core77	TAACCTCCTTAATTTTCATCTTCTGTTAGTATC
Frame4Turn_core78	TTCTTACCAGTATAAAGCAGAAAACTTTTTCAAATA
Frame4Turn_core79	CAAAGAACGCGCAACGCTCAACAGTAGGGCTTATTTTGCACC
Frame4Turn_core80	CAGCTACAATTAATTGAGCGCTAATATCAGAGAATCGCAAGA
Frame4Turn_core81	AAAGTCAGAGGGTTTATCCTGAATCTTACCA
Frame4Turn_core82	ACGATTTTTTGAAATTATTCATTAAAGGTGAATTATTGAGGGAG
Frame4Turn_core83	GGGAATTACGCCAAAGACAAAAGGGCGACATTCAACCGATCACCGTCA
Frame4Turn_core84	TAGCAAGGTTATTTTGTACAATCAATAGAAAATAAACGTAGA
Frame4Turn_core85	ACGGAATAAGTCCGGAACGTCACCAATGAAATGCCCCGTATA
Frame4Turn_core86	AACAGTTAATGAGTACCGCCACCCTCAGAACCCAAAGACACC
Frame4Turn_core87	ACCGTACTCAGGAGGTTTCCCCCTGCCTATTTTCGGA
Frame4Turn_core88	CATGAAAGAGTATAGCCCGGAATAGGATAGCA
Frame4Turn_core89	TTTTCTCTGAATTTGAAGGATTAGGATTAGCGGGGTTT
Frame4Turn_core90	TAGTGAATGACCGTGTGATAAATAAGGCGTTT
Frame4Turn_core91	GGTTTGAAATACCTTATCAAAATCATAGGTCTGAGAGACAAATCGTCGCTAT
Frame4Turn_core92	TATTTTAGGGCTTAGGTTGGGTTATATAACTATATGTAAATGCTAATGGAAA
Frame4Turn_core93	AATAATAAGAGCAAGAAAGAACACCCTGAAC
Frame4Turn_core94	TCAAAAATGAAAACAAAGTTACCAGAAGG
Frame4Turn_core95	AAACCGAGGAAACGCAAAATATTGACGGTTTAACG
Frame4Turn_core96	TTTCAACAGAACCGCCACCCTCAGAGCCACCACCCTCATTTTCAGGGTGTATC
Frame4Turn_core97	GTCTTTCCAGGAACCCATGTACCGTAACACTGAGTAAGTGCCGTCGA
Frame4Turn_core98	TTTTTTTGCTCAGTACCAGGCGGATTTTCGTCA
Frame4Turn_core99	GCGTAGATTTTTCAGGTTTACTTAGAATCCTTGAAAAGAGTCAA
Frame4Turn_core100	CATCGGGAATAACCTTGCTTCTGTTACCTTTT
Frame4Turn_core101	CATTTGAATTACCTTTTTTGATGCAAATCCAGATAACC
Frame4Turn_core102	CACAAGAATTGAGCATTTAACAATTT
Frame4Turn_core103	TTACCTGAAAAACAAAATTAATTATTAAGCCC
Frame4Turn_core104	AAATACATACATAAAGGCTAAAGGAATTGCGAAAAAAGGCT
Frame4Turn_core105	GAGAAATAGAAAGGAACAATGGCAACATATAA
Frame4Turn_core106	AAGAAACGGCCACCCTCAGTTTCAGCGGAGT
Frame4Turn_core107	AGCCCAATAGACGTTAGTAAATGAGTTGCGCC
Frame4Turn_core108	CCAGTACACCTCATAGTTAGCGTAATATATTCGGTCG

Frame4Turn_core109	ACAGAGGCCAACAACCATCGCCACGCATAACCGACGATCTAAAGTTTTGTC
Frame4Turn_core110	GATACCGATAATTTTCTGTATGGGATTTTGCTTAAACAGCTT
Frame4Turn_core111	CGGATTCGCCTTAAATCAATATATGTGAGTGAGAAACAATAA
Frame4Turn_core112	TAATTAATTTTCCACGTCAGATGAATATACAGTAACAGTCCTGATTG
Frame4Turn_core113	AAAAGTTTGTTAGAACCTACCATAAAGAAATT
Frame4Turn_core114	AGAAGGAGCGGAATTAAATTCATCAATATAATACCTTTTA
Frame4Turn_core115	GACAATGATTTGAGGACTAAAGACAAATACGTAATGCCAC
Frame4Turn_core116	CTGAGGCTTGCAGCCTCAGCAGCGAAAGAAATACACT
Frame4Turn_core117	GCAAAAGCAGCATCGGAACGAGGGTAGCAACGGCT
Frame4Turn_core118	TTTGGATTATACTTCTGAATAATGGAAGGGAGTAACA
Frame4Turn_core119	TATTTTGTATAGCCCTAAAACATCTCAAATAT
Frame4Turn_core120	GCTGAACCGCCATTAAAAATACCGAACGAACCACCAG
Frame4Turn_core121	CAGAAGATAGAACCCTTCTGACCTGAAAGCGTAAGTCCATCACGCAA
Frame4Turn_core122	ACAGAGATAAAACAGAGGTGAGGCCACGCTGAGAGCCAGC
Frame4Turn_core123	AATACTGCGGAATCGTCAGTTGGGAAGAAAAATCTACGTTAATAAAACACCA
Frame4Turn_core124	GAACGAGTAGTAAATTGGGCTTGAGATGGCTGACCTT
Frame4Turn_core125	AGGCTGGTTTAATTTCAACTTTAACTGGCT
Frame4Turn_core126	CATTATACCAGTCAGGACTAAATATTCATTGAATGAGAATGA
Frame4Turn_core127	AAAGCGCCATATTACCGCCAGCCACTACATTT
Frame4Turn_core128	AAAGGGACATTAGTAATAACATCACTTGCCTGACCAGTAATA
Frame4Turn_core129	AAACAGGAGCAATACTTCTTTGATTCTGGCCA
Frame4Turn_core130	GCCAGAATCCGAGTAAAAGAGTCTGAATACGTGGCACAGACAA
Frame4Turn_core131	GCTGCGCATTGCTTTGACGAACATATCGGCCTT
Frame4Turn_core132	GCTGGTAATATCCAGAACAATTGCGCCATTGAG
Frame4Turn_core133	CTTTCATCAACATGACGACGATAAAAACCAA
Frame4Turn_core134	AATAGCGAGAGGCAGACTTCAAAGTAGCCAG
Frame4Turn_core135	ACAGGTAGAAATTGCCAGAGGGGGTAATAGTACAACATTATT
Frame4Turn_core136	TAACGGAAAAATGTTTAGACTGGATTATAGTC
Frame4Turn_core137	CCAAAAGGTAACCCTCGTTTACCATAAATGTGAGCGAGTAAC
Frame4Turn_core138	TTTAGAGGACAGATGAACGGTGTACAGACCAAGGGAACCGAACTGAAAGTACAA
Frame4Turn_core139	AAAACACTTGTATCATCGCCTGACAGACGGTCAATCATAGGCGCAT
Frame4Turn_core140	TTATCATTATAGATAATACATTTGTTAGGAGCACTAACAAATCACCTT
Frame4Turn_core141	CAAACCCTGTTATCTAAAATATCTAGGATTTAGAAGTATTTTAATTTT
Frame4Turn_core142	CGGAGATTTCATCTTTGACCCCCAGCGATTATACCATTT
Frame4Turn_core143	TTTGTATTAAATCCTTTGCCCCGAACGTTAAGACTTTA
Frame4Turn_core144	CAAACAAAAGGAATTGAGGAAGCAATCAATATCTGGTCAGTTGGCAAATTT
Frame4Turn_core145	CATCAAGATAGCCGGAACGAGGCGTAAATTGTGTCGAAATCGAAAGAG
Frame4Turn_core146	TATTCATTACCCAAATGGCTTGCCCTGACGAGAAACGAAC
Frame4Turn_core147	TTTTCAACAGTTGATTGACAACCTCTTT
Frame4Turn_core148	TTTAGCGCGAAACACCAACTTTGAATTT

Table S7. Sequences of the adaptor staple strands (green-colored in Figure S7) composing the DNA origami frame.

Name	Sequence
Frame4Turn_Adap1	TCCCTGATTTAAGGTCCAGCCAGCTTCCGGCACCGCTTCCTGGCGAA
Frame4Turn_Adap2	CTCATTTTGGATTCTCCGTGGGAACAAACGGCGGATGTAGCAGGCGTCT
Frame4Turn_Adap3	AATTAACCAATGAAATAGCAATAGCTATCTTACCTCCGGCTTCATTG
Frame4Turn_Adap4	AATTGATGCTCACAAGACTCCTTATTACGCAGTATGTTAGCTCATATGG
Frame4Turn_Adap5	TCCCACGCCAATCCGAAGCCCTTTTAAAGAAAAGAGCACGAT
Frame4Turn_Adap6	GCCGAGGATTGGCGTGGGAATCGTGCTTCTGTCTC
Frame4Turn_Adap7	TATACCACCATTGCTTTCGAGGTGAATTTCTAAACAAC
Frame4Turn_Adap8	CGTTGAAGAAACAAACATCAAGGCAAAAGAAGATGATTATACGTC
Frame4Turn_Adap9	CAGTACAGATTGCTTTGAATACCGTCTTGCGCGTA
Frame4Turn_Adap10	AGTCAGCTTGCTACAAGTTACAAAATCGCGCAGATTTGTTTG
Frame4Turn_Adap11	AAGAACGTAGCAAGCTGACTCAAACAAAATACATTC
Frame4Turn_Adap12	AGCCTGGTTATCAGATGATGGCTCATCATATTCCTGATTCAATAC
Frame4Turn_Adap13	CGTCAGTTCGCCTGCAACAGTGCAGTATTAACACGTAAAAAT
Frame4Turn_Adap14	TGTGAGTTCTCAACATTCACCAGTCACACGAGTAGA
Frame4Turn_Adap15	GTCAGAACATGGATTATTTACATTGGCAGGAAGCACGTATCG
Frame4Turn_Adap16	CAGTGATAGTTCTGACCGATACGTGCTTCGTTGAGA
Frame4Turn_Adap17	CTCCGTTTCGCTCATGGAAATACTTGCAACAGGAAAAAATATCG
Frame4Turn_Adap18	TAGCACTGTCGGCCTCAGGAAGATCGCACTCATTCCATCCTC
Frame4Turn_Adap19	AAGAAGTTGATTCATCAGTTGAGAAGCGAGTCTCTGGA
Frame4Turn_Adap20	CGGAAACCCAGTGCTAGAGGATGGAATGACCTTAAA
Frame4Turn_Adap21	CCATAGACGACTAGCC
Frame4Turn_Adap22	CTGAGCGACCAAAAGAACTGGCATGATTATATTGGGAAGTTA
Frame4Turn_Adap23	TTGATACTCCTGTTTGACCGTAATGGGATAGGTCGTACGGGT
Frame4Turn_Adap24	GTCAACCCTTGAAAATCTCCAAAATAATAATTTTTTCACGGGATAAC
Frame4Turn_Adap25	GGCATATCTCGCTCAGTAACTTCCCAATATGTGAGC
Frame4Turn_Adap26	GCGGATACTGTATCGGTTTATCAGCTTGCACTAGATCTTGCG
Frame4Turn_Adap27	GCACTACGTTCATTAAACGGGTATTTTTTCATGAGGAAGTAGCTTAT
Frame4Turn_Adap28	GTGGGAGAGTATCCGCCGCAAGATCTAGTGCAATGG
Frame4Turn_Adap29	GAGATGCAGGAGAAGA
Frame4Turn_Adap30	CTCCCAACTCATTCACTGAATAACAACGTAACAAAGCTGATCGTTAA
Frame4Turn_Adap31	AAATTTGAAAACTTTAGGAATACCACATTCAACTTGAGGGC
Frame4Turn_Adap32	ACTCGCTGTTTTCGAAATTTGCCCTCAAGCGCGAGA
Frame4Turn_Adap33	TTGTTAGAAGAGCAACACTATCAAATTACGAGGCATAGTCTAGCGCA
Frame4Turn_Adap34	TGCTACAACAGGAGTATCAAACCCGTACAAAGGGAA

Table S8. Sequences of the staple strands (orange-colored in Figure S7) carrying the sticky ends, *b* stands for the blunt version of the staple, *stop* stands for stopper sticky ends used for the termination of tile assembly within frames. Different combinations were used to assign stick ends in a user-defined manner.

Name	Sequence
NW-1	ACTGAGGCTAGTCAGAGCCGTCATTGCGGAACAAAGAAACCACC
NW-2	ACTGAGTATTGAACCAGGCTTACGCCC
NW-3	ACTGAGAATGTATGGCGAATTATTCATTTCAA
NW-4	ACTGAGACGTATATTCAACGCAATGAA
NW-5	ACTGAGAGACAGATAAGCAGATAGCCGAATAGCAGCC
SW-1	AGCAAATGAAAAATCTAAAGCCTAATAGATTGTCTATGGTACCT
SW-2	ACTCACAATTTTACAACGTACGTACCT
SW-3	TGACGCTCAATCGTCTGAACTACACTGTACCT
SW-4	TCAGGGACGATATTAAACGGAGTACCT
SW-5	CCCAGTCAGGGGACGACGACAGTAGGTTTCCGTACCT
NE-1	TACGAAGGCACCAACCTAAAACCGCGACCTGCTGCATCTCAGGTA
NE-2	TGGTATAATAAGCTCGTAGTGCAGGTA
NE-3	CCAAAAGGAGCCTTTAATTCTCCACAGGTA
NE-4	ATCAATTGTTATCCGGGTTGACAGGTA
NE-5	GGAAGGTATAATAACGGAATACGATATGCCAGGTA
NW-1b	GGCTAGTCAGAGCCGTCATTGCGGAACAAAGAAACCACC
NW-2b	GTATTGAACCAGGCTTACGCCC
NW-3b	GAATGTATGGCGAATTATTCATTTCAA
NW-4b	GACGTATATTCAACGCAATGAA
NW-5b	GAGACAGATAAGCAGATAGCCGAATAGCAGCC
SW-1b	AGCAAATGAAAAATCTAAAGCCTAATAGATTGTCTATGG
SW-2b	ACTCACAATTTTACAACGTACG
SW-3b	TGACGCTCAATCGTCTGAACTACACTG
SW-4b	TCAGGGACGATATTAAACGGAG
SW-5b	CCCAGTCAGGGGACGACGACAGTAGGTTTCCG
NE-1b	TACGAAGGCACCAACCTAAAACCGCGACCTGCTGCATCTC
NE-2b	TGGTATAATAAGCTCGTAGTGC
NE-3b	CCAAAAGGAGCCTTTAATTCTCCAC
NE-4b	ATCAATTGTTATCCGGGTTGAC
NE-5b	GGAAGGTATAATAACGGAATACGATATGCC
SE-1b	TCTTCTCCTCCATGTTACTGTAATCTTGACAAGAACCGGA
SE-2b	TTAACGATTTGGGAGTCCAGAG
SE-3b	TCTCGCGCTAATGCAGATACATAACG
SE-4b	TGCGCTAGCTAACAAAGACGCC
SE-5b	TTCCCTTTACGTTGGTGTAGATGAAATTGT
SW-5stop	CCCAGTCAGGGGACGACGACAGTAGGTTTCCGTAC

NE-1stop	TACGAAGGCACCAACCTAAAACCGCGACCTGCTGCATCTCAGG
SE-1stop	AGTTCTTCTCCTCCATGTTACTGTAATCTTGACAAGAACCGGA
SE-5stop	AGTTTCCCTTTACGTTGGTGTAGATGAAATTGT

Table S9. Sequences of the biotinylated (cyan-colored in Figure S8), fluorophore anchoring (red-colored in Figure S8), and fluorophore modified (pink-colored in Figure S8) staple strands.

Name	Sequence
biotin-anchor-1	/5Biosg/TTTTTTTTTTATTTGGGGCGCGAGCTGTTAGCTATATTTCTTT
biotin-anchor-2	/5Biosg/TTTTTTTTTTAATTAGCAAAATTAAGCTAATAGTAGTAGCATTTT
biotin-anchor-3	/5Biosg/TTTTTTTTTTAACATCCAATAAATCATACAGGCAAGGCAAAAGTTT
biotin-anchor-4	/5Biosg/TTTTTTTTTTAAGAAAGCGAAAGGAGCGGGCAACGGTAC
biotin-anchor-5	/5Biosg/TTTTTTTTTTTGAACAAGAGAACGTGGCGAGAAAGGAAGGGTTT
atto-anchor-1	TTTGATTAAGACGCTGAGAACATAGCGATAGCTTATTTGAGATCCGACTACGC
atto-anchor-2	TTTGCATTCCACAGACAGCAACTACAACGCCTGTATTTGAGATCCGACTACGC
atto-anchor-3	TTTTTGCGGGATCGTCACGGAGTTAAAGGCCGCTTTTGAGATCCGACTACGC
atto-anchor-4	TTTCTTATGCGATTTTAAGAATCATTGTGAATTACTTTGAGATCCGACTACGC
atto-anchor-5	TTTATAATCAGTGAGGCCACCTGAGAAGTGTTTTTTTGAGATCCGACTACGC
atto-anchor-6	TTTAAACAGTTCAGAAAACCCCCCTCAAATGCTTTTTTGAGATCCGACTACGC
atto-anchor-7	TTTTTAATGCGCGAACTGAATGGCTATTAGTCTTTTGAGATCCGACTACGC
atto-anchor-8	TTTCGTAAAACAGAAATATCAAAATTATTTGCATTTGAGATCCGACTACGC
label-ATTO647N	/5ATTO647NN/AAGCGTAGTCGGATCTC

Table S10. Sequences of the photocleavable staple strands.

Name	Sequence
Adapt-NW-5-PC	GCCGGAGGATTGGCGTGGGAATCGTGCTTCTGTCTC/iSpPC/TCAGT
Adapt-NE-5-PC	TACCT/iSpPC/GGCATATCTCGCTCAGTAACTTCCCAATATGTGAGC
NW-5-HP-PC	TCAGT TTTTTT/iSpPC/ACTGAGAGACAGATAAGCAGATAGCCGAATAGCAGCC
NE-5-HP-PC	GGAAGGTATAATAACGGAATACGATATGCCAGGTA/iSpPC/TTTTTT TACCT

References

1. SantaLucia, J., Jr.; Hicks, D., The Thermodynamics of DNA Structural Motifs. *Annu. Rev. Biophys. Biomol. Struct.* **2004**, *33*, 415-440.
2. Jiang, S.; Hong, F.; Hu, H.; Yan, H.; Liu, Y., Understanding the Elementary Steps in DNA Tile-Based Self-Assembly. *ACS Nano* **2017**, *11*, 9370-9381.
3. Evans, C. G.; Hariadi, R. F.; Winfree, E., Direct Atomic Force Microscopy Observation of DNA Tile Crystal Growth at the Single-Molecule Level. *J. Am. Chem. Soc.* **2012**, *134*, 10485-10492.
4. Rothmund, P. W.; Papadakis, N.; Winfree, E., Algorithmic Self-Assembly of DNA Sierpinski Triangles. *PLoS Biol.* **2004**, *2*, e424.
5. Winfree, E. *Simulations of Computing by Self-Assembly*; CS-TR:1998.22; California Institute of Technology: Pasadena, CA, May 31, 1998.
6. Rothmund, P. W.; Ekani-Nkodo, A.; Papadakis, N.; Kumar, A.; Fygenson, D. K.; Winfree, E., Design and Characterization of Programmable DNA Nanotubes. *J. Am. Chem. Soc.* **2004**, *126*, 16344-16352.
7. Li, W.; Yang, Y.; Jiang, S.; Yan, H.; Liu, Y., Controlled Nucleation and Growth of DNA Tile Arrays within Prescribed DNA Origami Frames and Their Dynamics. *J. Am. Chem. Soc.* **2014**, *136*, 3724-3727.